A&A, 686, A289 (2024)
https://doi.org/10.1051/0004-6361/202449417

Astronomy & Astrophysics

PRODIGE – envelope to disk with NOEMA

III. The origin of complex organic molecule emission in SVS13A⋆

T.-H. Hsieh[1], J. E. Pineda[1], D. M. Segura-Cox[2,1,⋆⋆], P. Caselli[1], M. T. Valdivia-Mena[1], C. Gieser[1], M. J. Maureira[1], A. Lopez-Sepulcre[4,3], L. Bouscasse[3], R. Neri[3], Th. Möller[5], A. Dutrey[6], A. Fuente[7], D. Semenov[8], E. Chapillon[3], N. Cunningham[4], Th. Henning[8], V. Piétu[3], I. Jimenez-Serra[7], S. Marino[9], and C. Ceccarelli[4]

[1] Max-Planck-Institut für extraterrestrische Physik, Giessenbachstrasse 1, 85748 Garching, Germany
e-mail: thhsieh@mpe.mpg.de
[2] Department of Astronomy, The University of Texas at Austin, 2500 Speedway, Austin, TX, 78712, USA
[3] Institut de Radioastronomie Millimétrique (IRAM), 300 rue de la Piscine, 38406, Saint-Martin d'Hères, France
[4] Univ. Grenoble Alpes, CNRS, IPAG, 38000 Grenoble, France
[5] I. Physikalisches Institut, Universität zu Köln, Zülpicher Str. 77, 50937 Köln, Germany
[6] Laboratoire d'Astrophysique de Bordeaux, Université de Bordeaux, CNRS, B18N, Allée Geoffroy Saint-Hilaire, 33615 Pessac, France
[7] Centro de Astrobiología (CAB), CSIC-INTA, Ctra.deTorrejón a Ajalvir km 4, 28806, Torrejón de Ardoz, Spain
[8] Max-Planck-Institut für Astronomie, Königstuhl 17, 69117 Heidelberg, Germany
[9] Department of Physics and Astronomy, University of Exeter, Stocker Road, Exeter, EX4 4QL, UK

Received 30 January 2024 / Accepted 22 March 2024

ABSTRACT

Context. Complex organic molecules (COMs) have been found toward low-mass protostars, but the origins of the COM emission are still unclear. It can be associated with, for example, hot corinos, outflows, and/or accretion shock and disk atmospheres.
Aims. We aim to disentangle the origin of the COM emission toward the chemically rich protobinary system SVS13A using six O-bearing COMs.
Methods. We conducted NOrthern Extended Millimeter Array observations toward SVS13A as part of the PROtostars & DIsks: Global Evolution (PRODIGE) program. Our previous DCN observations reveal a possible infalling streamer, which may affect the chemistry of the central protobinary by inducing accretion outbursts and/or shocked gas. We further analyzed six O-bearing COMs: CH_3OH, aGg'-$(CH_2OH)_2$, C_2H_5OH, $CH_2(OH)CHO$, CH_3CHO, and CH_3OCHO. Although the COM emission is not spatially resolved, we constrained the source sizes to $\lesssim$0.3−0.4 arcsec (90−120 au) by conducting uv-domain Gaussian fitting. Interestingly, the high-spectral-resolution data reveal complex line profiles with multiple peaks; although the line emission is likely dominated by the secondary, VLA4A, at V_{LSR} = 7.36 km s^{-1}, the numbers of peaks (∼2−5), the velocities, and the linewidths of these six O-bearing COMs are different. The local thermodynamic equilibrium (LTE) fitting unveils differences in excitation temperatures and emitting areas among these COMs. We further conducted multiple-velocity-component LTE fitting to decompose the line emission into different kinematic components. As a result, the emission of these COMs is decomposed into up to six velocity components from the LTE modeling. The physical conditions (temperature, column density, and source size) of these components from each COM are obtained, and Markov chain Monte Carlo sampling was performed to test the fitting results.
Results. We find a variety in excitation temperatures (100−500 K) and source sizes (D ∼ 10−70 au) from these kinematic components from different COMs. The emission of each COM can trace several components, and different COMs most likely trace different regions.
Conclusions. Given this complex structure, we suggest that the central region is inhomogeneous and unlikely to be heated by only protostellar radiation. We conclude that accretion shocks induced by the large-scale infalling streamer likely exist and contribute to the complexity of the COM emission. This underlines the importance of high-spectral-resolution data when analyzing COM emission in protostars and deriving relative COM abundances.

Key words. line: formation – radiative transfer – ISM: kinematics and dynamics – ISM: molecules

1. Introduction

About 270 molecules have been found in the interstellar medium so far (Ceccarelli et al. 2022). Of these molecules, 40% are so-called interstellar complex organic molecules (COMs), defined as carbon-bearing molecules that have at least six atoms (Herbst & van Dishoeck 2009; Ceccarelli et al. 2017). COMs are commonly detected in massive star-forming regions (Blake et al. 1987; Gieser et al. 2023) and are also occasionally detected toward solar-type protostellar systems (Caselli & Ceccarelli 2012; van Dishoeck 2014, and references therein). In Class 0 protostars, COMs are seen in several cases, including IRAS 16293-2422 (van Dishoeck et al. 1995; Cazaux et al. 2003; Jørgensen et al. 2018), NGC 1333-IRAS 4A (Cazaux et al. 2003), and NGC 1333-IRAS 4B/IRAS2A (Bottinelli et al. 2007). COMs have even been detected toward pre-stellar cores (e.g., L1689B:

⋆ Based on observations carried out under project number L19MB with the IRAM NOEMA Interferometer. IRAM is supported by INSU/CNRS (France), MPG (Germany), and IGN (Spain).
⋆⋆ NSF Astronomy and Astrophysics Postdoctoral Fellow.

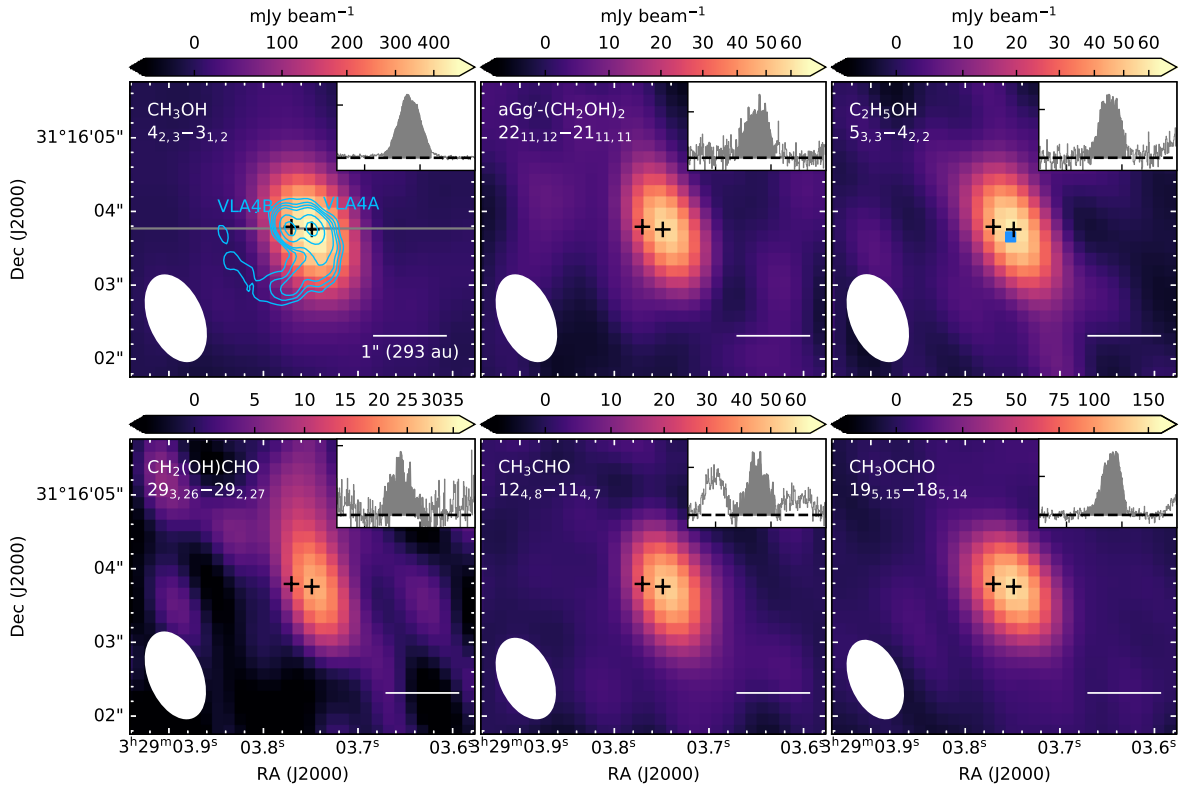

Fig. 1. Integrated intensity maps of a selected transition for each O-bearing COM. The top-right panel in each figure shows the spectra toward the center, and the filled regions indicate the integration range for the zero-order moment maps, which is 3.5−10.7 km s^{-1} (except for CH$_3$OH, for which it is 3.5−12.0 km s^{-1}), for the zero-order moment maps. The blue contours in the top-left panel represent the ALMA 1.3 mm continuum emission (Tobin et al. 2018) with levels of [3, 5, 7, 10, 30, 70]σ. The horizontal gray line in the top-left panel shows the PV cut used in Fig. 7. The blue pixel in the top-right panel is the pixel used to extract the spectra in this work.

Bacmann et al. 2012, L1544: Tafalla et al. 2006; Spezzano et al. 2016). Despite the wide variety of COMs and the types of objects in which they are found, we still have not yet fully characterized the origins of COM emission observationally.

In low-mass star-forming regions, COMs in the ice mantles of dust grains can sublimate into the gas phase in regions heated by the central protostars (>100 K). This zone is named the "hot corino", a compact source ($\lesssim$100 au) with high temperatures (>100 K) and high densities (>10^7 cm^{-3}; Caselli & Ceccarelli 2012; Ceccarelli et al. 2022). COMs are also found toward outflow cavity walls believed to be induced by shocks or protostellar UV irradiation (Jørgensen et al. 2004; Arce et al. 2008; Sugimura et al. 2011; Drozdovskaya et al. 2015; Palau et al. 2017). Furthermore, Oya et al. (2016) propose that at the centrifugal radius where the infalling material from the envelope lands on a protostellar disk, COMs can be liberated from dust mantles by weak accretion shocks in IRAS 16293-2422A. Similar scenarios are suggested by recent observations by Codella et al. (2018) and Vastel et al. (2022) toward HH212 and BHB2007 11, respectively. Belloche et al. (2020) categorized the COM emission in low-mass protostars into three groups: (1) hot corinos, (2) outflows, and (3) accretion shock and disk atmospheres.

Complex organic molecules are known to arise from SVS13A (Bianchi et al. 2017, 2019, 2022a,b; Lefloch et al. 2018; Belloche et al. 2020; Yang et al. 2021; Diaz-Rodriguez et al. 2022), a Class I protobinary system located in the NGC 1333 cluster within the Perseus Molecular Cloud (d = 293 pc; Ortiz-León et al. 2018). SVS13A contains two protostars, VLA4A and VLA4B, with a projected distance of 0.″3 (~90 au) based on the continuum observations (see the first panel of our Fig. 1 as well as Anglada et al. 2004; Tobin et al. 2016, 2018; Segura-Cox et al. 2018; Tychoniec et al. 2020). From multi-epoch observations, Diaz-Rodriguez et al. (2022) derived the total mass of the binary to be 1.0±0.4 $M_\odot$ using orbital motions (see also Maureira et al. 2020). By modeling the kinematics of the line emission, they further estimate stellar masses of 0.27±0.10 $M_\odot$ for VLA4A and 0.60±0.20 $M_\odot$ for VLA4B. The existence of a third hidden source at a distance of ~20−30 au from VLA4B is implied by the wiggling jets seen at large scales (Lefèvre et al. 2017). At least two spirals have been identified from the dust continuum emission (Diaz-Rodriguez et al. 2022), and they had been considered to be part of a fragmenting disk due to gravitational instability (Tobin et al. 2018). However, recent observations find that the dust spiral is connected to a larger-scale structure (at least 700 au) through a streamer traced by DCN emission, which perhaps delivers material from the envelope to the central system (Hsieh et al. 2023). Such infalling streamers at envelope scales have recently been identified toward several protostellar systems, which are suggested to funnel material near or into smaller-scale disks (Pineda et al. 2020, 2023; Alves et al. 2020; Ginski et al. 2021; Murillo et al. 2022; Cabedo et al. 2021; Garufi et al. 2022; Thieme et al. 2022; Valdivia-Mena et al. 2022). These infalling flows are believed to change the chemistry of the inner region (disk and/or inner envelope) by directly funneling material, inducing shock gas, and/or indirectly triggering protostellar outbursts. For SVS13A, the high luminosity, $L_{\rm bol}$ = 45.3 $L_\odot$, suggests that it is undergoing a protostellar accretion outburst. This makes SVS13A a good candidate for studying the chemical inventory under the influence of an accretion burst.

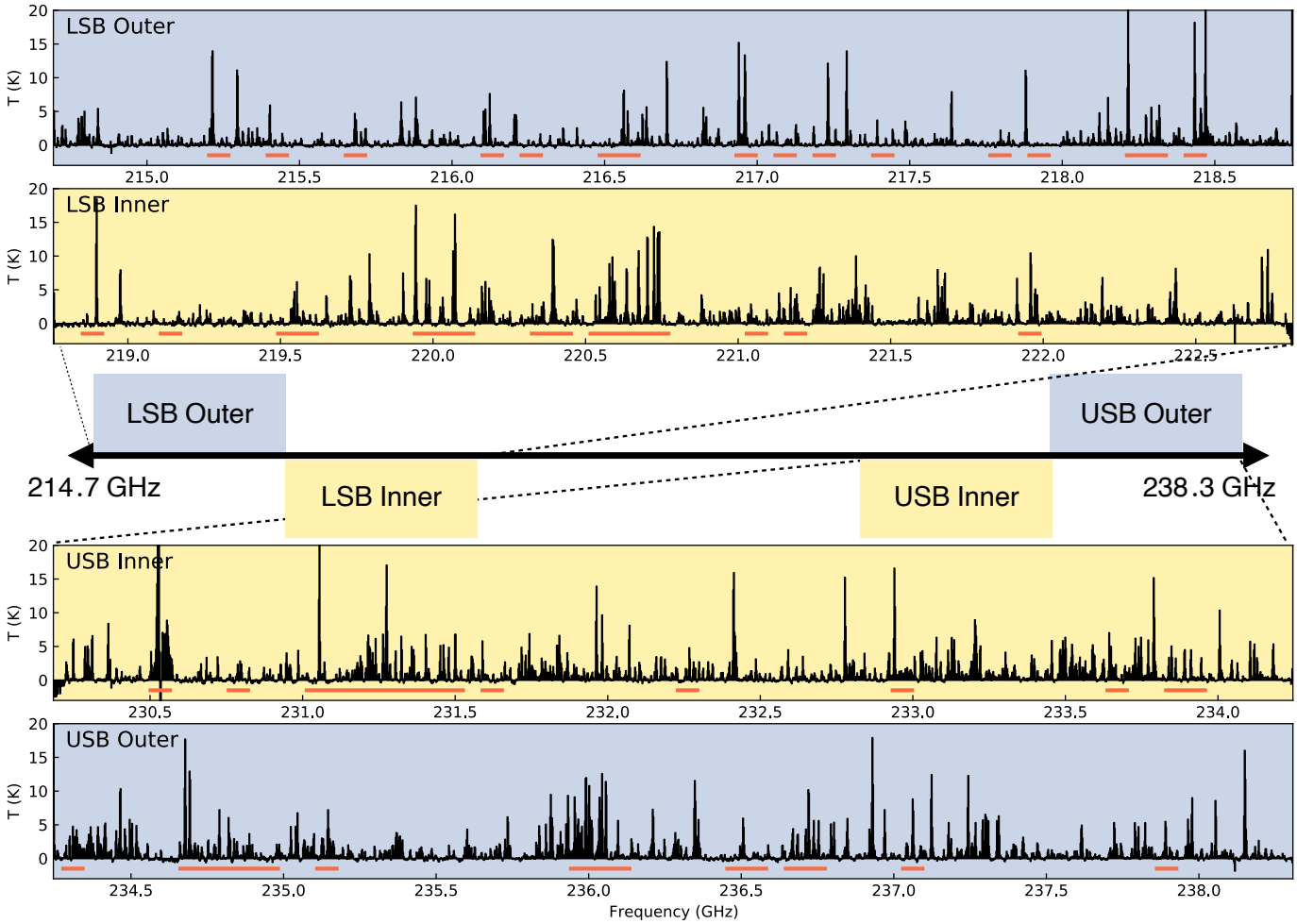

Fig. 2. Low-spectral-resolution spectrum toward the continuum peak of SVS13A from the PRODIGE NOEMA large program. The panels, from top to bottom, represent the spectra from the receiver bands as shown in the sketch in the middle. The horizontal orange bars represent locations of the high-spectral-resolution windows.

In this paper we present new NOrthern Extended Millimeter Array (NOEMA) data at 1.3 mm toward SVS13A. We selected six oxygen-bearing (O-bearing) COMs (CH_3OH, aGg'-$(CH_2OH)_2$, C_2H_5OH, $CH_2(OH)CHO$, CH_3CHO, and CH_3OCHO) that are found to be relatively bright with complex line profiles (multiple peaks) in our data; O-bearing COMs are also suggested to be more abundant relative to CH_3OH in shock regions (Csengeri et al. 2018, 2019). CH_3OCH_3 is also detected but in only a few blended transitions, preventing a detailed kinematic analysis (Appendix C). This work focuses on disentangling the kinematics of the protostellar system to determine from which structures the COM emission originates, taking advantage of the high spectral resolution and broadband capabilities of the Institut de Radioastronomie Millimétrique (IRAM) NOEMA PolyFiX correlator. In Sect. 2 we describe the observations and calibration. The results are presented in Sect. 3. In Sect. 4 we detail the analysis, and we discuss our findings in Sect. 5. Our conclusions are summarized in Sect. 6.

2. Observations

The observations were carried out with NOEMA at IRAM. It is part of the MPG-IRAM observing program PROtostars & DIsks: Global Evolution (PRODIGE; Project ID: L19MB002, PIs: P. Caselli and Th. Henning). The observations are briefly described in Hsieh et al. (2023) that reports the data of C_8^1O $J = 2-1$, DCN $J = 3-2$, and CH_3CN $J = 12_k-11_k$ (K = 0–7).

In this paper we present the data covering six O-bearing COMs: CH_3OH, aGg'-$(CH_2OH)_2$ (the most stable conformer of $(CH_2OH)_2$, Christen et al. 2001), C_2H_5OH, $CH_2(OH)CHO$, CH_3CHO, and CH_3OCHO. Here we describe the receiver setups with the PolyFiX correlator. The receiver contains four broadband dual polarization low-resolution windows and 39 narrowband high-resolution windows. The broadband windows cover 214.7−218.8 GHz, 218.8−222.8 GHz, 230.2−234.2 GHz, and 234.2−238.3 GHz with a channel width of 2 MHz (~2.7 km s^{-1}). The 39 narrowband windows are distributed within the mentioned ranges with a channel width of 62.5 kHz (Fig. 2). The resulting spectral resolutions of the narrowband windows are ~0.078−0.086 km s^{-1}.

Self-calibration was performed with solution intervals of 300, 135, and 45 s on the broadband data as in Hsieh et al. (2023). The solutions are then applied to the broadband and narrowband data. Imaging was done using the GILDAS/`MAPPING` package[1].We used the `clean` task with natural weighting in order to get the best sensitivity. This gives beam sizes of 1.″11 × 0.″67 to 1.″24 × 0.″73 with a rms noise level of ~0.5 K

[1] https://www.iram.fr/IRAMFR/GILDAS

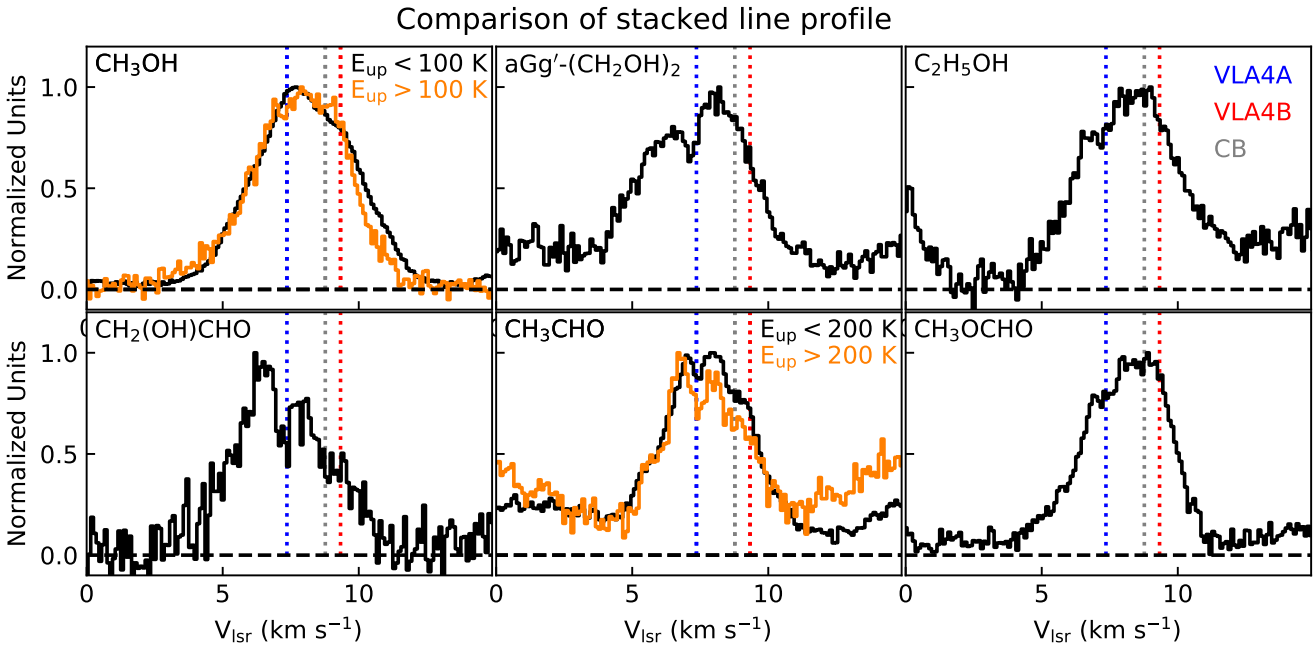

Fig. 3. Comparison of stacked line profiles of the six O-bearing COMs. The stacking was done using spectra normalized to their peak fluxes and weighting with the reciprocal of noise squared (Appendix A). The vertical dashed lines indicate the central velocities of the disks of VLA4A (blue), 4B (red), and the circumbinary disk (gray) from Diaz-Rodriguez et al. (2022).

at a resolution of ∼0.8 km s−1. Given the large number of channels in both the broadband data and the high-spectral-resolution datasets, we did not clean using a support mask, and a shallow clean of the whole image with a 5σ threshold was performed, where σ is the rms noise level. The single-point spectra toward the continuum peak (pixel at α = $3^{h}29^{m}$ $03^{s}.75$, δ = $31^{d}16^{m}03^{s}.73$) were extracted for analysis.

3. Results

3.1. Line identification

Figure 2 shows the full NOEMA spectrum from the broadband low-resolution data toward the continuum peak. Line identification is first conducted using the `LineIdentification` function of the eXtended CASA Line Analysis Software Suite (XCLASS) package, which automatically identifies lines, derives a quantitative description of each identified species, and return the corresponding physical parameters including the temperature, column density, source size, linewidth and systemic velocity (XCLASS, Möller et al. 2017) with the full broadband windows covering 16 GHz. We disentangle the complicated line profiles using high-spectral-resolution data in a later section.

3.2. Stacking of lines

In order to increase the signal of the multiple peak structures, we stacked the spectra from selected transitions for each COM; we manually selected several transitions that are less contaminated by others. To be selected, the transition is expected to be broadly consistent with the XCLASS modeling result in amplitudes and share similar linewidths and spectral profiles (Sect. 3.1). Columns 7 in Tables B.1 to B.6 list the transitions that were stacked (see Appendix A and Fig. A.1). The spectra were first interpolated to the same grid using the SciPy package (Virtanen et al. 2020). The spectra were then normalized by the peak flux and averaged with a weight of the inverse of square noise (σ'; i.e., the noise after normalization) using NumPy (Van Der Walt et al. 2011):

$$T_{\rm bri,stack}(v) = \frac{\sum_{i=0}^{N} T_i(v) \times \frac{1}{\sigma'^2_i}}{\sum_{i=0}^{N} \frac{1}{\sigma'^2_i}}. \quad (1)$$

The stacked line profiles help confirm multiple peaks in complex line profiles; we note that these lines have different opacities and energy levels, so their profiles are not necessary the same. For $CH_2(OH)CHO$, $(CH_2OH)_2$, and C_2H_5OH, there are limits of selected transitions or similar E_{up} in the range 40–450 K for $CH_2(OH)CHO$, 110−266 K for aGg'-$(CH_2OH)_2$, 23−409 K for C_2H_5OH, and 129−207 K for CH3OCHO for CH_3OCHO. The stacked profile are broadly similar to the individual spectral profile (Fig. A.1). For CH_3OH, we split the transitions with E_{up} in the ranges 45−96 K and 775−802 K to stack. CH_3CHO have 13 selected transitions and were split into ones with 81−128 K and ones with 287−490 K. Since the stacked line profile reveals a complex line profile, we need a model to disentangle the kinematic components from it.

Figure 3 shows the stacked line profiles for the six selected O-bearing COMs toward the continuum peak. It shows that different COMs have multiple peaks at different velocities, suggesting that they trace different kinematic components in the system. In comparison to the systemic velocities of VLA4A/4B and the circumbinary disks, a dip is shown roughly at the velocity of VLA4A for the selected O-bearing COMs, with the exception of CH_3OH. For CH_3CHO, it seems a second dip at the systemic velocity of the circumbinary disk. These differences also support that these molecules trace different kinematic components. These kinematic components are likely associated with the physical structures, for example, the disk, shocks, streamer, or the outflow. aGg'-$(CH_2OH)_2$ shows a double peak structure likely tracing the rotating disk or envelope of VLA4A. This is consistent with the results from high-angular-resolution

Table 1. Emitting components based on spectra and location.

	aGg′-$(CH_2OH)_2$		C_2H_5OH		$CH_2(OH)CHO$		CH_3CHO		CH_3OCHO	
Based on	Spectra	Spatial	Spectra	Spatial	Spectra	Spatial	Spectra	Spatial	Spectra	Spatial
VLA4A	✓	✓	✓	✓	✓	✓	✓	✓	✓	✓
VLA4B	✗	✗	?	✗	✗	✗	?	✗	?	✗
Circumbinary	?	✗	✓	✓	?	✗	✓	✗	✓	✓

Notes. The contributed components based on the stacked line profiles ("spectra"; see Sect. 3.2) and uv-domain Gaussian fitting ("spatial"; see Sect. 3.4).

Atacama Large Millimeter/submillimeter Array (ALMA) observations (Diaz-Rodriguez et al. 2022) that aGg'-$(CH_2OH)_2$ only traces the disk around VLA4A. A double peak profile centered toward VLA4A is also seen in $CH_2(OH)CHO$. However, $CH_2(OH)CHO$ is narrower and its blueshifted peak is brighter while the opposite is true for aGg'-$(CH_2OH)_2$. On the other hand, C_2H_5OH, CH_3OCHO, and CH_3CHO emission contains more than two peaks, which likely trace not only the VLA4A disk but also the circumbinary disk and/or VLA4B and perhaps streamers, shocks, inner envelopes, etc. These results are summarized in Table 1.

3.3. Gaussian widths and velocities

To first examine the different physical structures a molecule traces, we conducted Gaussian fitting to the line profiles (narrowband) of each selected transition from the six O-bearing COMs. The transitions are listed in Tables B.1–B.6.

Figure 4 shows a comparison of the best-fit linewidths and the central velocities of these spectral-line profiles with a single Gaussian. Although we have a limited number of uncontaminated transitions, it is clear that the linewidths and central velocities are different between the O-bearing COM species. This suggests that these COMs can be associated with different kinematic components in the protobinary system SVS13A. Considering the central velocities, it is likely that $CH_2(OH)CHO$, aGg'-$(CH_2OH)_2$, and CH_3CHO emission is dominated by VLA4A while CH_3OH, C_2H_5OH, and CH_3OCHO likely have significant emission coming from the circumbinary disk (and perhaps VLA4B).

3.4. Spatial distribution of COM emission

To derive properties of the gas traced by the COM emission, it is crucial to know the source size. Figure 1 shows the integrated intensity maps of the six selected O-bearing COMs. All of them show point-source like structure given the spatial resolution of $\sim 1\farcs2 \times 0\farcs7$ (~300 au). The deconvolved source sizes from the uv-domain Gaussian fitting ($\lesssim 0\farcs3$, 90 au) are smaller than the beam size, suggesting that they are point sources at the current resolution. This gives an upper limit of the emitting regions of ~90 au. More discussions on the source sizes are provided in Sects. 4.1 and 4.2. The compact sources might rule out the possibility that the emission comes from larger-scale structures, such as irradiated cavity walls carved by the bipolar outflows.

The peak positions of line emission are used to indicate the most likely location of the emitting gas at specific velocity, especially for optically thin lines (Sargent & Beckwith 1987; Harsono et al. 2013). Toward SVS13A, Hsieh et al. (2023) conducted a uv-domain Gaussian fitting to CH_3CN emission using a channel width of 0.5 km s^{-1}, and found a velocity gradient from west to

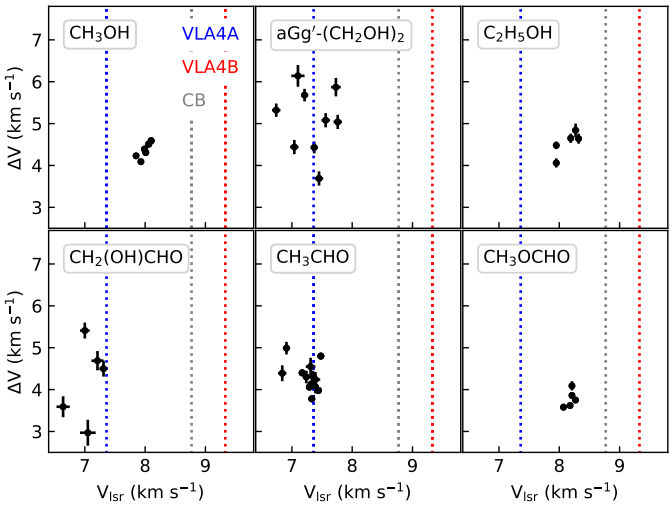

Fig. 4. Gaussian linewidth versus central velocity of the selected transitions from the six O-bearing COMs. The vertical dashed lines represent the central velocities of the disks of VLA4A (blue), 4B (red), and the circumbinary disk (gray). The transitions in use are listed in Tables B.1–B.6.

east (Fig. 5, top panel); the visibility data are first resampled to a width of 0.5 km s^{-1}, and `uv_fit` task in `MAPPING` is used to conduct the 2D Gaussian fit for each channel. We applied the same technique to six O-bearing COMs in SVS13A with the selected transitions (From Tables B.1 to B.6). This revealed the spatial weighting centers of each velocity for each transition.

The O-bearing lines have lower S/Ns compared to the CH_3CN emission, especially in the red- or blueshifted wings. For uv-plane fitting of the O-bearing COM emission, we only considered data points with $S/N > 7$ and position uncertainty $<0\farcs5$. Figure 5 shows the fitted central positions. It is noteworthy that, for each molecule, although the transitions have different upper energy levels and opacities (Tables B.1–B.6), the spatial distributions are similar. It is clear that the emission of these O-bearing COMs originates from different locations in the system. CH_3OH, C_2H_5OH, and CH_3OCHO show a velocity gradient with the direction consistent with that of CH_3CN. These three molecules also share similar systemic velocity ~8.1 km s^{-1} from the line profile fitting (Fig. 4). However, the redshifted end of CH_3OCHO extends close to VLA4B while the CH_3OH is relatively compact and likely dominated by VLA4A. For aGg'-$(CH_2OH)_2$, $CH_2(OH)CHO$, and CH_3CHO, the line emission most likely comes from VLA4A. This agrees with the results from line stacking except for CH_3CHO, which has 3–4 components (Fig. 3). However, considering their Gaussian peak velocity, these molecules have emission dominated by VLA4A (Fig. 4). We summarize them in Table 1.

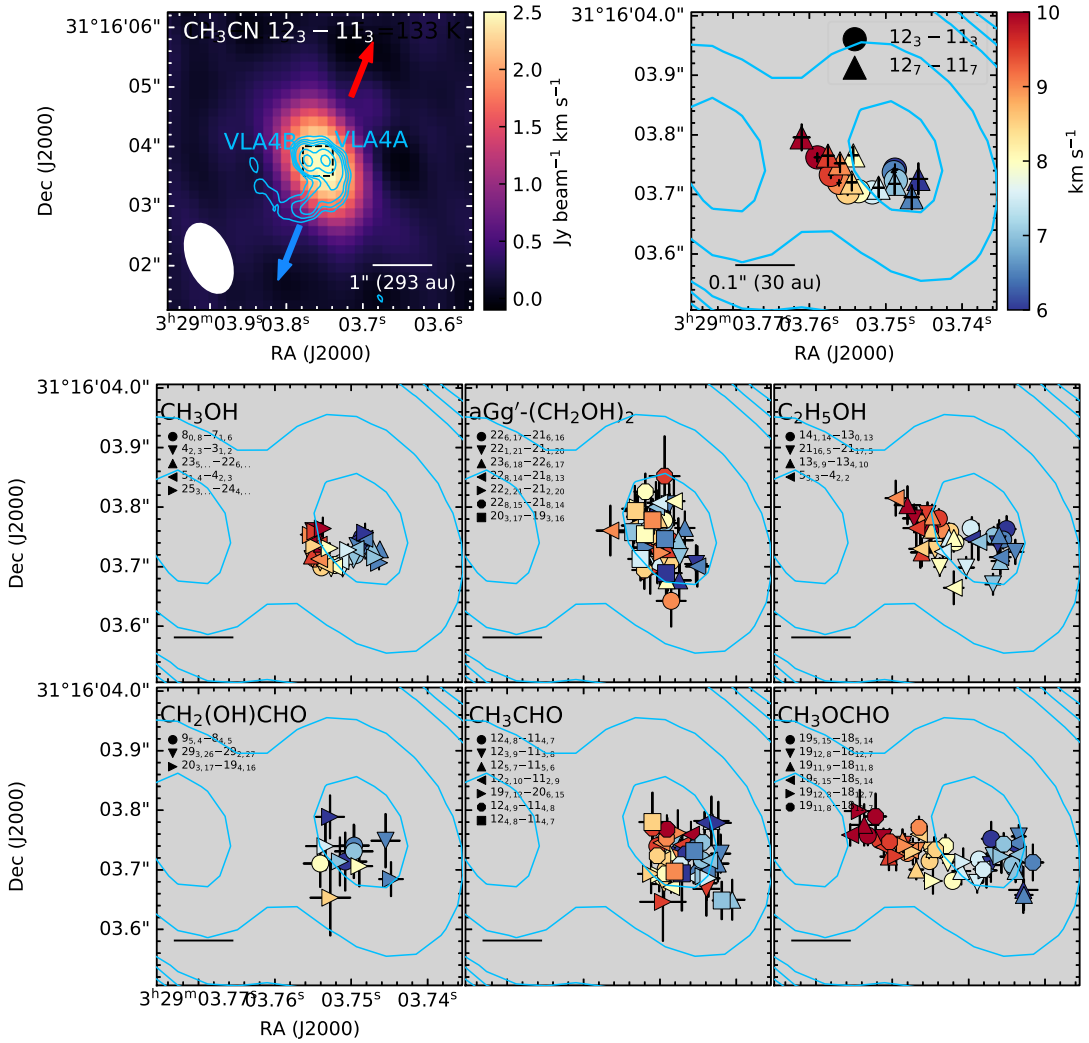

Fig. 5. Central positions of selected COM transitions at different velocities. The top two panels show the integrated intensity map (left) and central positions (right) from CH_3CN (Hsieh et al. 2023) as a reference for the O-bearing COMs. The contours show the 1.3 mm continuum emission from Tobin et al. (2018). Different line transitions are marked with different symbols (Tables B.1–B.6). The scale bar is 0.″1 for the bottom six panels. The beam sizes for these COM emissions depend on the line frequency but are the same as that of CH_3CN (1.″2 × 0.″7) within 10%.

4. Analysis

4.1. One-component LTE Gaussian model

We applied radiative transfer modeling to the emission of selected transitions of the six O-bearing COMs. Though multiple peaks are found in the line profiles from the high-spectral-resolution data (Fig. 3.2), we first performed local thermodynamic equilibrium (LTE) modeling of the spectra with one Gaussian velocity component. We used the LTE approach as the collisional rate coefficients of COMs are only available in a few COMs (e.g., from the Leiden Atomic and Molecular Database[2]). This one component model provides the first-order estimate of the physical conditions of the gas traced by each COM molecule; we use multiple Gaussian component modeling to decompose the complex structures in Sect. 4.2. Non-LTE analysis had already been done for CH_3OH (Bianchi et al. 2017: $n_{H_2} > 10^8$ cm^{-3}) and CH_3CN (Hsieh et al. 2023: $n_{H_2} \sim 6.2 \times 10^6$ cm^{-3} and $n_{H_2} > 1.2 \times 10^8$ cm^{-3} with two components). These analyses, for the only two COMs with known collision coefficients, suggest that COMs come from the central dense regions, implying that LTE analysis is reasonable for other COMs.

We applied the model to fit the high-spectral-resolution spectra extracted from the position of the peak continuum emission. The NOEMA observations at 1.3 mm cover ~200–1400 transitions, depending on the species (Fig. 2). At the same time, line contamination from nearby transitions becomes a severe issue to model the line profiles (Fig. 2). We therefore checked the line profiles from all transitions covered in the high-spectral-resolution data for each molecule. We selected as many transitions as possible with a range of line strengths and upper energy levels to better constrain the physical conditions (Tables B.1–B.6). The selection process is done by iteratively checking the model and line profiles of all transitions located in the narrow band windows. Based on the XCLASS model (Sect. 3.1, fitting the low-spectral-resolution data with the latest and most complete list of molecules), a transition that is contaminated by different molecules is first removed. A line emission much higher than the model profile may be also considered as contaminated by unidentified lines. In the other word, the final (one-velocity-component) model of the high-spectral-resolution data is broadly consistent with the XCLASS model considering more channels

[2] https://home.strw.leidenuniv.nl/~moldata/

but fewer transitions. Line contamination can also be treated by masking the specific, overlapping velocity ranges so that more transitions can be included (Figs. B.1–B.6). Unlike line stacking (Sect. 3.2), the fit includes line profiles with several overlapping transitions from the same molecule (see below). In addition, undetected transitions can be included as they help constrain the physical conditions, especially when the transition has a high Einstein coefficient and/or low upper energy level.

We constructed a LTE-radiative transfer model to fit the line profiles of the selected transitions. The model includes five free parameters: column density ($N_{\rm tot}$), excitation temperature ($T_{\rm ex}$), central velocity ($V_{\rm LSR}$), linewidth (ΔV), and source size ($\Omega_{\rm S}$). We note here the linewidth is set to a free parameter as one value for all transitions. This intrinsic linewidth is for $\tau(v)$ so that it should be smaller than the real linewidth in the optically thick transitions. The line opacity as a function of velocity (frequency) was first constructed following the XCLASS manual[3] (Möller et al. 2017):

$$\tau(v) = \sum_{\rm i} \tau_{\rm i,peak} \exp\left(-\frac{(v - V_{\rm LSR})^2}{2\sigma^2}\right), \tag{2}$$

where

$$\tau_{\rm peak} = \frac{A_{\rm ul} c^3}{8\pi\nu^3 \Delta V \frac{(\pi ln2)^{1/2}}{2}} N_{\rm u}(e^{h\nu/kT_{\rm ex}} - 1), \tag{3}$$

for which i indicates the transition in use, $\sigma \sim \frac{\Delta V}{2\sqrt{2\ln 2}}$, $A_{\rm ul}$ is the Einstein coefficient, c is light speed, and ν is the rest frequency of the transition from the Cologne Database for Molecular Spectroscopy (CDMS[4]; Müller et al. 2005; Endres et al. 2016). $N_{\rm u}$ is the column density at the upper energy state and can be expressed as

$$N_{\rm u} = N_{\rm tot} \frac{g_{\rm u}}{Q(T_{\rm ex})} e^{-E_{\rm u}/kT_{\rm ex}}, \tag{4}$$

where $g_{\rm u}$ is the degeneracy, $Q(T_{\rm ex})$ is the partition function, and $E_{\rm u}$ is the upper energy level. Finally, the line intensity is constructed as

$$I_\nu(v) = \frac{\Omega_{\rm S}}{\Omega_{\rm B}} (J_\nu(T_{\rm ex}) - J_\nu(T_{\rm bg}))(1 - \exp(-\tau(v))), \tag{5}$$

where $\Omega_{\rm S}$ and $\Omega_{\rm B}$ are the source size and beam size, respectively, and $T_{\rm bg} = 2.7$K. We note that $\Omega_{\rm B} = 1\farcs2 \times 0\farcs7$ as we first scaled the intensity of the observed spectra to this beam size for convenience.

We conducted the fitting using the SciPy `curve_fit` method[5] to estimate initial parameter values. Then, `emcee` (Foreman-Mackey et al. 2013) was used to perform Markov chain Monte Carlo (MCMC) sampling using the parameters from `curve_fit` estimates with uniform distribution for priors. The resulting best-fit parameters are listed in Table 2 (they are the ones marked as having a "single" component). The fitted parameters and their uncertainties were taken with relevant 16, 50, and 84% quantiles (Hogg & Foreman-Mackey 2018). We find that each O-bearing molecule probes gas with different physical conditions. The excitation temperatures are from ∼145 K (C_2H_5OH) to ∼240 K (aGg'-$(CH_2OH)_2$) and the source sizes vary from ∼0.″10 (aGg'-$(CH_2OH)_2$) to ∼0.″28 ($CH_2(OH)CHO$). This again suggests that these COMs come from different components/regions of this protobinary system.

Figures B.1–B.6 show the best-fit in use (Tables B.1–B.6). Transitions with optically thick emission are crucial to break the degeneracy between the source size and the column density (e.g., $\Omega_{\rm S}$ and τ in Eq. (5)). On the other hand, to determine the temperature, transitions covering a broad range of energy levels are necessary. Figure B.7 shows the τ of the best-fit model as a function of $E_{\rm u}$ for the transitions in use. We used this figure to evaluate the fitting results. For example, $CH_2(OH)CHO$ fitting was done using only optically thin lines ($\tau \lesssim 0.13$); in such a case, Eq. (5) is approximately $I_\nu(v) \propto \Omega_{\rm S}\tau(v)$. Hence, τ, which is proportional to the column density of the energy state (Eq. (3)), is degenerate with source size; this results in an unconstrained posterior distribution in the MCMC sampling. We note that although the column density cannot be constrained, the intensity ratios can still reflect the temperature in the optically thin case. In addition, the total amount of molecules can be estimated (i.e., Col. 8 in Table 2).

4.2. Multi-velocity component LTE Gaussian model

The line profiles of these O-bearing COMs usually contain multiple peaks (Fig. 3). This suggests that one COM can trace or several kinematic components, and different COMs can trace different regions in SVS13A. The multiple components do not trace the same material. Therefore, we performed multi-velocity-component fitting to disentangle the physical conditions traced by the line profiles. For CH_3OH, we did not conduct multiple component fitting as only a few transitions are observed and the energy levels of $E_{\rm up}$ from 100−700 K are not present in our setup.

The multiple-velocity-component model setup is the same as that of the one-component model (Sect. 4.1) but with more Gaussian components. The fitting is using the same spectra with selected transitions and mask to the one-velocity-component case (Sect. 4.1). Each component has its own physical parameters so that one adds five additional free parameters ($T_{\rm ex}$, $\log N_{\rm tot}$, ΔV, $V_{\rm LSR}$, size) for each additional velocity component added to the model. We assumed these components are spatially separated and do not interact.

To decide how many velocity components are needed to fit the line emission, we employed the Akaike information criterion (AIC) AIC $= 2k + \chi^2 + C$, where k is the number of the free parameters and χ is the classical chi-squared statistic (see also Choudhury et al. 2020; Valdivia-Mena et al. 2022). In our case, k is equal to 5 times the number of components. Thus, by adding one velocity component, χ^2 needs to decrease by 10 to compensate AIC. A small AIC is in favor for the model. We conducted χ^2 fitting starting with one component, and adding components one by one until the ΔAIC does not significantly change (Table 3). The details are described in Appendix B. This process to decide the number of velocity components was done using gradient-based optimization (SciPy `curve_fit`) with less computational expense than with the MCMC method.

After deciding the number of components, we performed the MCMC sampling. The Markov chains start from positions surrounding the best-fitting model in high-dimensional space with uniform priors; tens of walkers (depending on the k) were running simultaneously using the "Stretch Moves" in `emcee` (Goodman & Weare 2010; Foreman-Mackey et al. 2013). The initial values were set to the nearby the best-fit model from `curve_fit`. As with the one-component model (Sect. 4.1), the best-fit parameters and the uncertainties were taken with

[3] http://cassis.irap.omp.eu/docs/RadiativeTransfer.pdf
[4] https://cdms.astro.uni-koeln.de/cdms/portal/
[5] https://scipy.org/citing-scipy/

Table 2. Physical conditions of COMs from MCMC sampling.

COM	Component	T_{ex} (K)	log N_{tot} (cm^{-2})	ΔV (km s^{-1})	V_{LSR} (km s^{-1})	D (diameter) (arcsec)	$N_{tot} \times$ area$^{(a)}$ (cm^{-2} arcsec^2)	$\frac{N_X}{N_{CH_3OH}}$ $^{(b)}$	$\frac{[X]}{[CH_3OH]}$ $^{(c)}$
CH_3OH	Single	$229.3^{+0.72}_{-0.64}$	$18.9^{+0.01}_{-0.01}$	$3.12^{+0.01}_{-0.01}$	$8.05^{+0.01}_{-0.01}$	$0.279^{+0.001}_{-0.001}$	$1.95^{+0.01}_{-0.01} \times 10^{18}$	1	1
aGg′-$(CH_2OH)_2$	Single	$240.6^{+14.0}_{-13.15}$	$18.17^{+0.04}_{-0.04}$	$3.85^{+0.06}_{-0.06}$	$7.55^{+0.02}_{-0.02}$	$0.1^{+0.003}_{-0.003}$	$4.69^{+0.53}_{-0.53} \times 10^{16}$	0.186	0.024
aGg′-$(CH_2OH)_2$	Comp 1	$278.7^{+62.06}_{-46.59}$	$18.05^{+0.18}_{-0.16}$	$1.48^{+0.07}_{-0.07}$	$5.68^{+0.08}_{-0.08}$	$0.057^{+0.006}_{-0.006}$	$1.16^{+0.54}_{-0.54} \times 10^{16}$	–	0.036
	Comp 2	$184.9^{+16.46}_{-15.28}$	$17.68^{+0.07}_{-0.08}$	$2.5^{+0.12}_{-0.13}$	$8.16^{+0.05}_{-0.05}$	$0.112^{+0.005}_{-0.005}$	$1.89^{+0.38}_{-0.38} \times 10^{16}$	–	–
	Comp 3	$471.4^{+201.4}_{-118.9}$	$19.22^{+0.36}_{-0.28}$	$6.03^{+0.46}_{-0.42}$	$7.52^{+0.2}_{-0.17}$	$0.027^{+0.006}_{-0.006}$	$3.92^{+3.72}_{-3.72} \times 10^{16}$	–	–
C_2H_5OH	Single	$97.53^{+1.81}_{-1.74}$	$17.44^{+0.02}_{-0.02}$	$3.88^{+0.04}_{-0.04}$	$8.24^{+0.02}_{-0.02}$	$0.254^{+0.005}_{-0.004}$	$5.56^{+0.37}_{-0.37} \times 10^{16}$	0.035	0.029
C_2H_5OH	Comp 1	$87.03^{+2.75}_{-2.76}$	$17.3^{+0.04}_{-0.04}$	$3.12^{+0.12}_{-0.11}$	$7.53^{+0.1}_{-0.1}$	$0.233^{+0.008}_{-0.008}$	$3.4^{+0.37}_{-0.37} \times 10^{16}$	–	0.032
	Comp 2	$142.7^{+24.51}_{-15.36}$	$17.7^{+0.19}_{-0.14}$	$2.75^{+0.16}_{-0.13}$	$9.72^{+0.1}_{-0.1}$	$0.134^{+0.019}_{-0.021}$	$2.84^{+1.52}_{-1.52} \times 10^{16}$	–	–
$CH_2(OH)CHO$	Single	$151.9^{+2.4}_{-2.97}$	$16.86^{+0.29}_{-0.36}$	$4.49^{+0.12}_{-0.12}$	$7.04^{+0.04}_{-0.04}$	$0.268^{+0.132}_{-0.072}$	$1.64^{+2.11}_{-2.11} \times 10^{16}$	0.009	0.008
$CH_2(OH)CHO$	Comp 1	$115.3^{+31.2}_{-20.18}$	$17.43^{+0.22}_{-0.27}$	$0.81^{+0.18}_{-0.13}$	$6.22^{+0.07}_{-0.06}$	$0.07^{+0.011}_{-0.009}$	$4.09^{+2.84}_{-2.84} \times 10^{15}$	–	0.010
	Comp 2	$134.8^{+109.8}_{-44.95}$	$15.58^{+0.75}_{-0.58}$	$0.68^{+1.93}_{-0.27}$	$8.09^{+0.36}_{-0.11}$	$0.155^{+0.097}_{-0.08}$	$2.88^{+6.16}_{-6.16} \times 10^{14}$	–	–
	Comp 3	$149.7^{+3.74}_{-3.79}$	$16.98^{+0.24}_{-0.19}$	$4.78^{+0.18}_{-0.17}$	$7.18^{+0.07}_{-0.07}$	$0.223^{+0.051}_{-0.05}$	$1.49^{+1.07}_{-1.07} \times 10^{16}$	–	–
CH_3CHO	Single	$154.6^{+1.33}_{-1.25}$	$17.12^{+0.01}_{-0.01}$	$3.41^{+0.01}_{-0.02}$	$7.76^{+0.01}_{-0.01}$	$0.252^{+0.002}_{-0.002}$	$2.62^{+0.06}_{-0.06} \times 10^{16}$	0.017	0.013
CH_3CHO	Comp 1	$143.3^{+5.38}_{-4.99}$	$16.83^{+0.04}_{-0.04}$	$0.99^{+0.04}_{-0.04}$	$6.74^{+0.02}_{-0.02}$	$0.16^{+0.007}_{-0.008}$	$5.42^{+0.74}_{-0.74} \times 10^{15}$	–	0.019
	Comp 2	$105.4^{+12.32}_{-10.74}$	$16.22^{+0.08}_{-0.1}$	$0.5^{+0.03}_{-0.03}$	$7.95^{+0.01}_{-0.01}$	$0.127^{+0.008}_{-0.007}$	$8.4^{+2.13}_{-2.13} \times 10^{14}$	–	–
	Comp 3	$116.5^{+2.58}_{-2.63}$	$16.73^{+0.03}_{-0.03}$	$2.29^{+0.06}_{-0.06}$	$8.43^{+0.04}_{-0.04}$	$0.242^{+0.004}_{-0.004}$	$9.91^{+0.84}_{-0.84} \times 10^{15}$	–	–
	Comp 4	$133.9^{+12.2}_{-10.87}$	$16.58^{+0.05}_{-0.05}$	$0.8^{+0.04}_{-0.04}$	$5.51^{+0.03}_{-0.03}$	$0.123^{+0.005}_{-0.005}$	$1.8^{+0.27}_{-0.27} \times 10^{15}$	–	–
	Comp 5	$182.0^{+11.99}_{-10.85}$	$18.09^{+0.07}_{-0.07}$	$5.14^{+0.17}_{-0.16}$	$7.85^{+0.06}_{-0.06}$	$0.069^{+0.004}_{-0.004}$	$1.82^{+0.36}_{-0.36} \times 10^{16}$	–	–
CH_3OCHO	Single	$173.6^{+2.05}_{-2.03}$	$17.44^{+0.01}_{-0.01}$	$3.53^{+0.01}_{-0.01}$	$8.17^{+0.01}_{-0.01}$	$0.348^{+0.002}_{-0.002}$	$1.05^{+0.03}_{-0.03} \times 10^{17}$	0.035	0.054
CH_3OCHO	Comp 1	$134.4^{+14.87}_{-12.21}$	$17.24^{+0.1}_{-0.09}$	$0.65^{+0.04}_{-0.04}$	$6.81^{+0.02}_{-0.02}$	$0.136^{+0.015}_{-0.015}$	$1.01^{+0.33}_{-0.33} \times 10^{16}$	–	0.079
	Comp 2	$111.3^{+6.48}_{-6.1}$	$17.01^{+0.05}_{-0.06}$	$1.13^{+0.07}_{-0.07}$	$7.52^{+0.04}_{-0.05}$	$0.214^{+0.012}_{-0.012}$	$1.47^{+0.25}_{-0.25} \times 10^{16}$	–	–
	Comp 3	$116.2^{+7.87}_{-7.72}$	$17.15^{+0.05}_{-0.06}$	$1.54^{+0.08}_{-0.07}$	$9.62^{+0.07}_{-0.07}$	$0.202^{+0.014}_{-0.013}$	$1.8^{+0.34}_{-0.34} \times 10^{16}$	–	–
	Comp 4	$168.6^{+18.13}_{-15.37}$	$17.11^{+0.13}_{-0.16}$	$1.25^{+0.1}_{-0.09}$	$5.88^{+0.06}_{-0.05}$	$0.16^{+0.021}_{-0.014}$	$1.04^{+0.46}_{-0.46} \times 10^{16}$	–	–
	Comp 5	$133.8^{+7.49}_{-6.81}$	$17.36^{+0.05}_{-0.04}$	$1.45^{+0.06}_{-0.06}$	$8.59^{+0.05}_{-0.05}$	$0.209^{+0.012}_{-0.014}$	$3.13^{+0.54}_{-0.54} \times 10^{16}$	–	–
	Comp 6	$179.3^{+19.18}_{-16.13}$	$18.93^{+0.09}_{-0.08}$	$3.81^{+0.19}_{-0.19}$	$8.15^{+0.11}_{-0.11}$	$0.051^{+0.005}_{-0.004}$	$7.03^{+1.88}_{-1.88} \times 10^{16}$	–	–

Notes. For each molecule, we provide the best-fit parameters for the one-component LTE model (Sect. 4.1) denoted as single in the second column and for the multi-velocity component LTE model (Sect. 4.2) denoted as comp x in the second column. $^{(a)}$The area is derived as πr^2 where r is $D/2$. $^{(b)}$The column density ratio with respect to CH_3OH. $^{(c)}$The abundance ratio with respect to CH_3OH derived from the $N_{tot} \times$ area, i.e., Col. 8. For multiple-velocity case, the $N_{tot} \times$ area from each component are sum up.

Table 3. Multicomponent model comparison.

	aGg′-$(CH_2OH)_2$		C_2H_5OH		$CH_2(OH)CHO$		CH_3CHO		CH_3OCHO	
Num. of components	χ^2	ΔAIC	χ^2	ΔAIC	χ^2	ΔAIC	χ^2	ΔAIC	χ^2	ΔAIC
1	12 993	0	39 843	0	4911	0	11 379	0	11 323	0
2	12 865	−118	39 774	−59	4888	−13	10 840	−529	10 428	−885
3	12 773	−82	(39 751)	(−13)	4824	−54	10 443	−387	10 234	−184
4	(12 753)	(−10)	–	–	(4802)	(−12)	10 329	−104	9991	−233
5	–	–	–	–	–	–	10 083	−236	9713	−268
6	–	–	–	–	–	–	(10 054)	(−19)	9563	−140
7	–	–	–	–	–	–	–	–	(9534)	(−19)

Notes. ΔAIC is in comparison with the previous level. The brackets around the final rows indicate the stop point at which ΔAIC (as well as χ^2) do not significantly change; therefore, the model in previous row is taken.

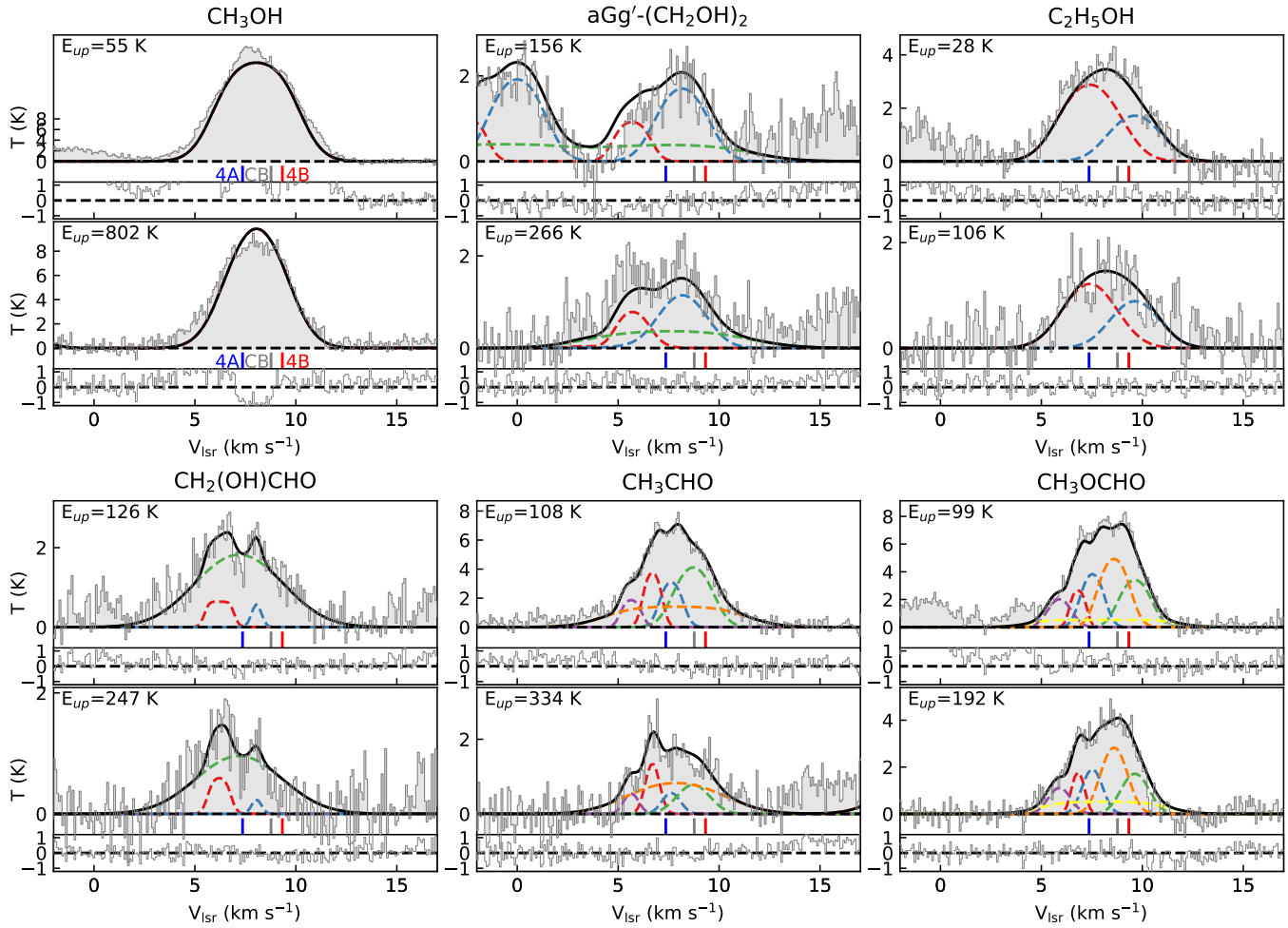

Fig. 6. Spectral profiles of two selected transitions for each O-bearing COM. The black curve shows the best-fit model with multiple kinematic components, and the colored dashed lines represent the contribution from each component. The blue, red, and gray bars at the bottom indicate the systemic velocities of VLA4A, VLA4B, and the circumbinary disk, respectively. The insets at the bottom of each panel show the residual from the best-fit model.

16, 50, and 84% quantiles (Hogg & Foreman-Mackey 2018). Table 2 shows these results, and Fig. 6 shows the best-fit models for each COM in two selected transitions that have different upper energy levels and relatively high S/N among the transitions in use for fitting. We find that for a given species, the line emission can consist of several components with different temperatures. The temperatures are different from the single-component fitting by $\lesssim$30% except for aGg'-$(CH_2OH)_2$, for which the three-component fitting yields temperatures of 180−470 K in comparison to the 240 K by the one-component model.

It is important to discuss how opacity affects the fitting process. In the fitting process, the line interaction between components is not included, that is to say, each velocity component is assumed to be spatially separated. In C_2H_5OH and CH_3OCHO, the velocity components are relatively offset from each other so that the opacity effects are small in the overlapping region. In aGg'-$(CH_2OH)_2$, CH_3CHO, and $CH_2(OH)CHO$, a broad-line component is found. This component overlaps with the others. For $CH_2(OH)CHO$, based on the single component fitting, the line emission of the broad-line component is most likely optically thin in the best-fit model (Fig. B.7). For aGg'-$(CH_2OH)_2$ and CH_3CHO, it is likely that their broad-line components include some optically thick transitions in the fitting. These broad-line components with higher column density and small source sizes might be associated with the central compact regions (see also Sect. 4.3). If this is the case, this compact emission is behind the extended sources. Thus, the physical conditions of the spatially compact broad-line components are inaccurate while the remaining components are less affected. This is, however, the limit of the dataset. Higher-angular-resolution data are required to resolve these issues.

4.3. Comparison with high-angular-resolution data

The multicomponent fitting reveals several kinematic components. Though the best-fit model has been checked (Fig. 6), we further evaluated the fitting results using high-angular-resolution data. We compared the central velocity, linewidth, and source size from the best-fit with the high-angular-resolution data. aGg'-$(CH_2OH)_2$, CH_3CHO, and CH_3OCHO emission was detected with ALMA at an angular resolution of $\sim$0.″20 × 0.″11 and PA = −0.9° ($\sim$30−60 au; Diaz-Rodriguez et al. 2022).

Figure 7 shows the position-velocity (PV) diagrams from two selected transitions of aGg'-$(CH_2OH)_2$, CH_3CHO, and CH_3OCHO in the high resolution data, for which the PV cut is taken in the east–west direction through VLA4A and VLA4B (Fig. 1). Here we compare the best-fit V_{LSR}, ΔV, and sizes with the PV diagrams. In the PV diagram, we plot an ellipse

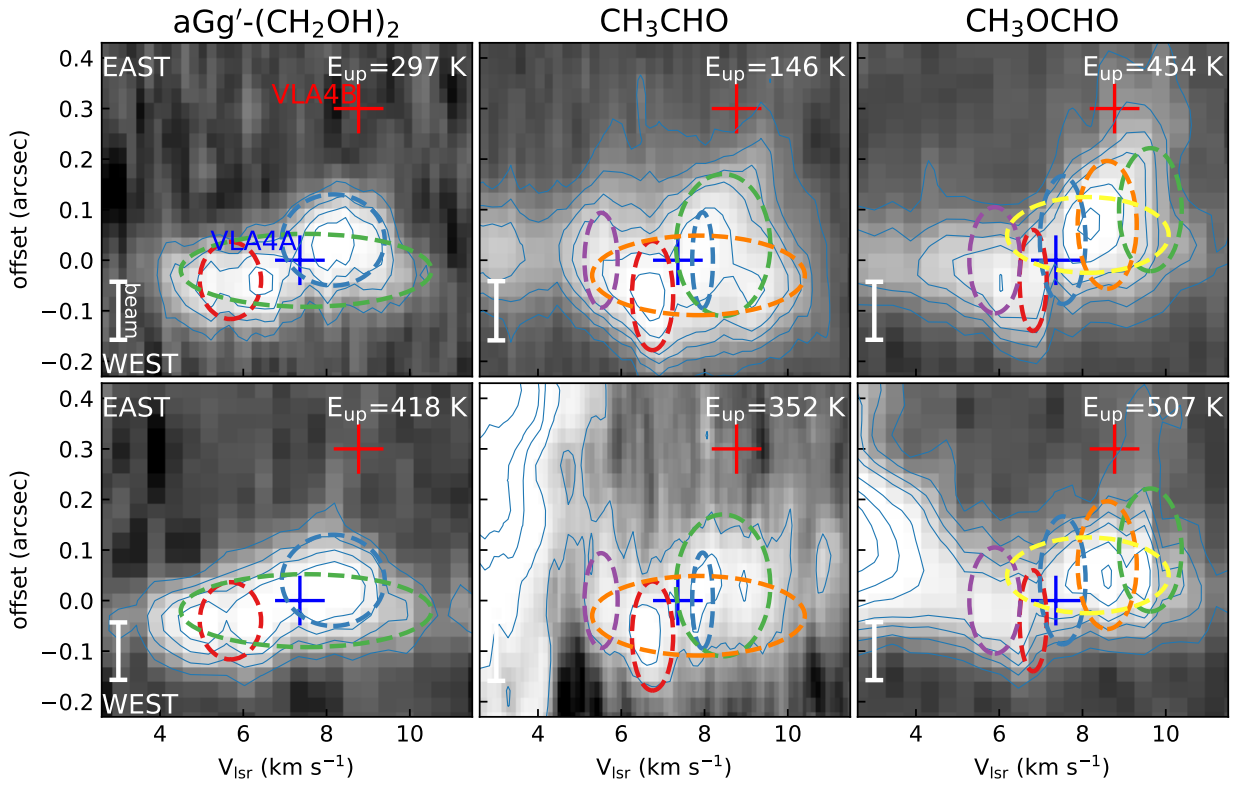

Fig. 7. PV diagrams of aGg'-$(CH_2OH)_2$, CH_3CHO, and CH_3OCHO from high-angular-resolution ALMA data (Diaz-Rodriguez et al. 2022). The dashed colored ellipses represent each kinematic component from the best-fit model (with the same colors as Fig. 6). The blue and red crosses indicate the positions and velocities of VLA4A and VLA4B, respectively. The white bar in the lower-left corner shows the beam size along the PV cut. NOEMA fits on top of the higher-resolution ALMA data match the structure, validating the NOEMA fit results.

representing each kinematic component from the best-fit model. The width, height, and x-axis location correspond to the ΔV, source sizes, and $V_{\rm LSR}$. The y-axis offsets of ellipses were manually adjusted by eye. The height of the ellipse is given by $(\text{size}^2 + \text{beam}_{\rm EW}{}^2)^{1/2}$, where $\text{beam}_{\rm EW}$ is the beam size along the east–west PV cut. While the $V_{\rm LSR}$ and ΔV can be directly seen in the spectral profiles (Fig. 6), the source size is obtained based on the line intensity ratios from multiple transitions with their opacities τ. In other words, an accurate source size suggests a good τ correction with a reasonable column density as well as the temperature. As a result, each component from the lower-spatial-resolution NOEMA data is a relatively good match of the components seen in the high-spatial-resolution ALMA data, suggesting reasonable fitting of the NOEMA data at least for the three COMs, aGg'-$(CH_2OH)_2$, CH_3CHO, and CH_3OCHO. Again, the broad-line components in aGg'-$(CH_2OH)_2$ and CH_3CHO can be ambiguous; the best-fit source sizes for the broad-line component, 0.″034 and 0.″083, are smaller than the beam of the ALMA observation. In such a case, the ALMA data do not resolve these components and only provide an upper limit to their source size. For the other components, derived source sizes are also on the same order of, or smaller than, the beam of the ALMA observations.

5. Discussion

5.1. Sizes of the O-bearing COM emission

To probe the origin of COM emission, it is crucial to estimate the size of the emitting area. The origin of COM emission can be roughly categorized into three groups: (1) hot corinos, (2) outflows, and (3) accretion shock and disk atmospheres (Belloche et al. 2020).

With the uv-domain Gaussian fitting, we find that, in our NOEMA observations at an angular resolution of 1.″2 × 0.″7 (350 × 200 au), the COM emission is a point-source like. This means it is unlikely that this emission traces the outflow cavity walls, which are usually extended.

Expected from the bolometric luminosity of SVS13A 44 $L_\odot$, Belloche et al. (2020) estimate a radius of >40 au where the temperature is about the sublimation temperature of COMs ∼100–150 K. Because this size is similar to the size of COM emission (see also Hsieh et al. 2019, 2023), Belloche et al. (2020) classify the COM emission in SVS13A as a hot corino.

With the LTE model of one Gaussian component (Table 2), we derived the full width at half maximum size of each COM emission: 0.″11 (31 au for aGg'-$(CH_2OH)_2$), 0.″25 (74 au for CH_3CHO), 0.″25 (74 au for C_2H_5OH), 0.″22 (65 au for CH_3OCHO), and 0.″31 (92 au for $CH_2(OH)CHO$). These sizes are derived based on a number of transitions covering optically thin to thick emission (except for $CH_2(OH)CHO$; see Appendix B), providing an estimate of source size independent of the angular resolution of the observation (see also Sect. 4.3). These source sizes are within the sublimation radius (∼30−80 au for 150−100 K) estimated by Belloche et al. (2020), but different O-bearing COMs trace different sizes (r = 16−45 au). Intuitively, one might speculate that it is due to different sublimation temperatures of COMs or different chemical processes at work in different locations of the source; a trend of the decreasing temperature with increasing radius from ∼30−8000 au is found using the derived source sizes and temperatures from molecules (Fig. 9 in Bianchi et al. 2022a). The derived $T_{\rm ex}$ with source sizes

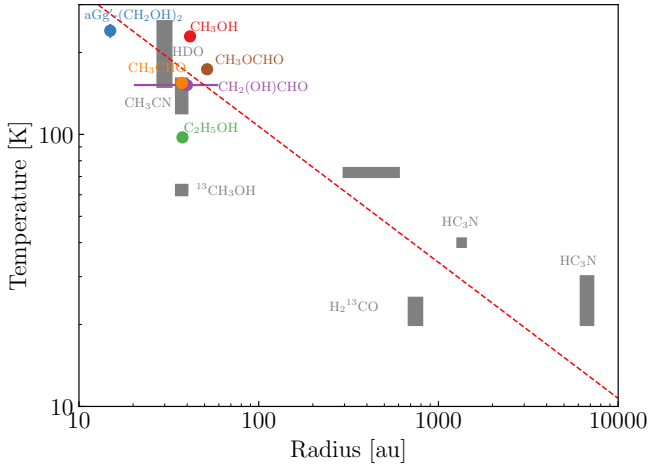

Fig. 8. Figure 9 from Bianchi et al. (2022a) with data points of COMs from this work.

(radius) are consistent with the correlation found in Bianchi et al. (2022a). With COM emission on smaller scales, we do not seen a clear trend with the limited number of data points (Fig. 8).

5.2. Complex structures

5.2.1. Kinematics

The six O-bearing COMs show different profiles (Fig. 3), suggesting that they come from different regions within the SVS13A system. Although the emission is not spatially resolved, their Gaussian centers at different velocities further support this scenario (Fig. 5).

Among the six O-bearing COMs, we found velocity gradients from the west to the east in CH_3OH, C_2H_5OH, CH_3CHO, and CH_3OCHO, while aGg'-$(CH_2OH)_2$ and $CH_2(OH)CHO$ emission do not show a velocity gradient. For aGg'-$(CH_2OH)_2$, it is consistent with the ALMA high-resolution observations by Diaz-Rodriguez et al. (2022) in which the aGg'-$(CH_2OH)_2$ emission only traces the VLA4A disk. The double-peak line profiles around the V_{LSR} of VLA4A (Fig. 3) from aGg'-$(CH_2OH)_2$ and $CH_2(OH)CHO$ also imply that their emission is dominated by a rotating disk/inner envelope of VLA4A. For the other four COMs, although the velocity gradients share a similar direction from the west to the east, they have indeed different slopes. The fitted Gaussian centers may be considered as a flux-weighted centroid in a case of unresolved extended emission at the given velocity. Therefore, together with the multiple-peak spectral profiles (Fig. 3), we speculate that the emission of these four COMs traces not only the VLA4A disk but also the VLA4B disk and/or the circumbinary disk although the VLA4A disk likely dominates it based on both the velocity and spatial information. Even for CH_3OCHO with the most extended structure (Fig. 5), the redshifted emission near the V_{LSR} = 9.33 km s^{-1} is located around the mid-point of VLA4A and VLA4B. This is also consistent with the high-angular-resolution ALMA data (Fig. 7).

Complex organic molecule emission with different optical depths can trace different layers, as we found for $CH_3{}^{13}CN$ and CH_3CN (Hsieh et al. 2023). In the case of protostellar envelopes, intuitively, the optically thick lines of COMs should trace the outer region while the thin transitions should trace the inner dense region. It is more complicated in Fig. 5 as each velocity step has a different optical depth. Thus, we should see the spatial distribution from low to high velocity goes across from optically thin (wing) to optically thick (middle) and back to optically thin (wing). In this case, in additional to the optically thin transitions, the blue- and redshifted line wing should point toward the center. However, this is unlikely the case; the most optically thick line of CH_3OH ($\tau_{1comp.}$ = 7.3, Table B.1), likely traces the inner region where a large velocity gradient is present (Fig. 5), while the CH_3OCHO emission is associated with the outer region with $\tau_{1comp.}$ = 0.6−1.7 (Table B.6). Alternatively, if the COM emission comes from a disk, it is possible the optically thick emission lines trace the inner part of the disk where the density and temperature are high. However, as mentioned in Sect. 3.4, the spatial distributions are similar from different transitions with different optical depths for each COM (Fig. 5). This suggests that the discrepancy seen in the COM distribution most likely originate from chemical, rather than optical depth effects.

5.2.2. Physical conditions

Traditionally, to derive physical conditions of the gas traced by COMs, rotation diagrams and/or simple one-component Gaussian models are used. It is, however, frequently seen in rotation diagrams that multiple components exist with different temperatures (slopes) when many transitions cover wide ranges of energy levels. With this in mind, to robustly derive the physical conditions, we need to first identify the kinematic components with high-angular-resolution and high-spectral-resolution data with as many transitions as possible. However, this is usually very time expensive in observations.

The abundance ratios relative to CH_3OH or other species, for example [X]/CH_3OH, have been commonly used to study the chemical composition (e.g., Calcutt et al. 2018; Belloche et al. 2020; Jørgensen et al. 2020; Yang et al. 2021). The abundance ratios ($\frac{[X]}{[CH_3OH]}$ from one-velocity model, Table 2) toward SVS13A are slightly different by a factor of 0.5–2.6 to the column density ratios derived by Belloche et al. (2020) except for aGg'-$(CH_2OH)_2$ with a factor of 4. In Belloche et al. (2020), the column density is derived based on the rotation diagram under an assumption of source size of 0.″3 (Table 5 in the paper). For aGg'-$(CH_2OH_2$, the difference is likely caused by a very different rotational temperature 98 K from Belloche et al. (2020) and 240 K in this work. Here, we have included transitions with $E_{up} \gtrsim$ 300 K as Belloche et al. (2020) use transitions with E_{up} < 250 K (Fig. E.29 in the paper). In the multiple-velocity component fitting, we find a possible component with a rotation temperature of 470 K that is dominant among the molecule. This explains the difference in the abundance ratio of aGg'-$(CH_2OH)_2$ (i.e., $\frac{[aGg'-(CH_2OH)_2]}{[CH_3OH]}$) derived from Belloche et al. (2020) and this work. However, toward SVS13A, it is clear that COMs are associated with different structures. Unless the COM emission is both spectrally and spatially resolved, the discussion of abundance ratios can mix together contributions of distinct structures, providing no quantitative physical constraints needed for chemical models.

Our NOEMA observations cover a number of transitions for modeling at a high-spectral-resolution (Tables B.1–B.6). Thus, multiple kinematic components can be disentangled and their physical conditions can be derived (Table 2; see also Hsieh et al. 2023 for CH_3CN). Figure 9 shows the temperature of these kinematic components as a function of velocity (Table 2). For the one-component model, it unveils that the different O-bearing COMs are tracing different regions with different temperatures and source sizes. The multicomponent fitting further unveils several components with temperatures ranging

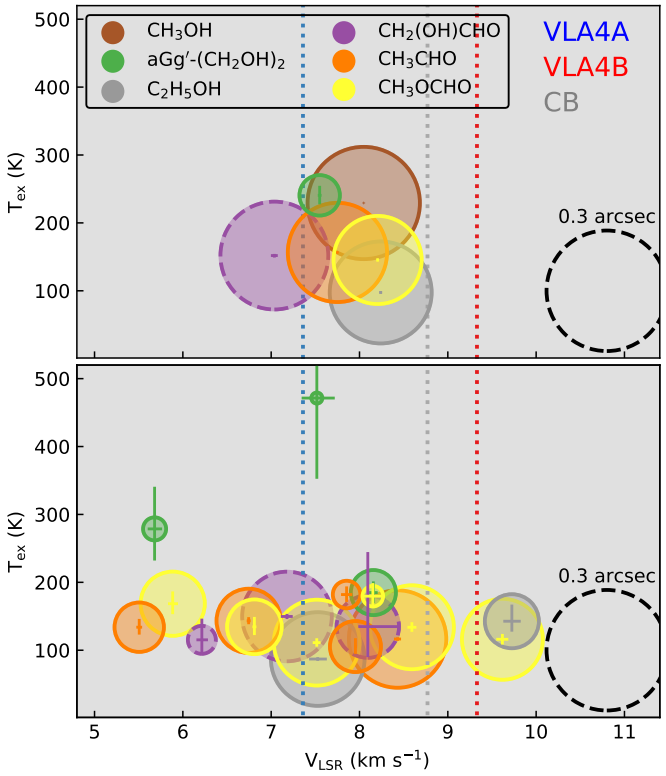

Fig. 9. Excitation temperature as a function of central velocity for the six O-bearing COMs. The top panel shows the results from single component fitting, and the bottom panel shows the results from the multicomponent fit. The size of the circle represents the source size; the $CH_2(OH)CHO$ circle has a dashed outline since the source size of $CH_2(OH)CHO$ can be degenerate with column density due to a lack of optically thick transition. The dashed circle at the bottom-right corner indicates a size of 0.3 arcsec.

from a few tens to a few hundred kelvin. It is likely that the one-component model usually gives a temperature between those derived from multiple-component model. However, the total amount of molecules (i.e., N_{tot}×area in Table 2) is always higher in multiple-component fitting; the sum of the N_{tot}×area from the multiple-component fitting is larger than that of single component fitting by a factor of 1.1−1.5 (see $\frac{[X]}{[CH_3OH]}$ in Table 2. That is because the multiple-component fitting process may unveil hidden components from the complex line profile (Hsieh et al. 2023). Also, these components are assumed to be spatially separated so that the integrated τ from the multi-velocity model can be larger than that of the single component.

5.3. Origin of COM emission in SVS13A

Thanks to the capabilities of the NOEMA PolyFiX correlator, we have identified multiple velocity components toward SVS13A, and better quantified the kinematics and physical conditions using six O-bearing COMs. It is clear that the COM emission traces different kinematic components toward SVS13A with different physical conditions (temperature, column density and size). This suggests that the COM emission in SVS13A originates from a complex structure, which may not be explained by a unique scenario.

It is interesting to compare with the well-studied hot corino protobinary system IRAS 16293-2422A (hereafter IRAS 16293A) at an earlier evolutionary stage than SVS13A (Pineda et al. 2012; Jørgensen et al. 2016; Ceccarelli et al. 2022). With high-angular-resolution ALMA observations, Maureira et al. (2020) found complex structures toward IRAS 16293A traced by HNCO, NH_2CHO, and t−HCOOH. Maureira et al. (2022) find that these complex structures are associated with hot dust and gas spots (see also Oya & Yamamoto 2020). The kinematic, spatial distribution, and temperature were in agreement with predictions from shocks. Shocks are expected, for example, due to the landing of inalling streamers in the disk high-density material. Indeed, an infalling streamer inducing local shocks has been found by Garufi et al. (2022) via SO toward a more evolved young stellar object HL Tau (see also van Gelder et al. 2021); an infalling streamer toward IRAS 16293A is also suggested by Murillo et al. (2022). This hints at a scenario where the physical and chemical properties of an inner region ($\lesssim$300 au) is affected by large-scale (approximately a few thousand au) infalling streamers (see Pineda et al. 2023 and references therein).

Toward SVS13A, Hsieh et al. (2023) suggest that the continuum spiral structure connected to VLA4A is associated with a streamer from larger scales, which is possibly infalling. Bianchi et al. (2022b) speculate that streamer-induced shocks sputter icy COMs from dust grains given the asymmetric structure of COM emission toward SVS13A from high-angular-resolution data. In this work, we find that the COM emission traces complex structures, so it is unlikely only due to heating from the central protostellar source. Thus, we consider that shocks from materials infalling onto and impacting circumstellar or circumbinary disks play an important role in feeding COMs from dust grains, leading to the complex structure in COM emission. Other possibilities are shocks produced by the self-gravity or tidal forces within the disks themselves. To understand this requires high-angular-resolution observations, coupled with high spectral resolution and sensitivity.

6. Conclusion

We present NOEMA observations toward SVS13A of six selected O-bearing COMs. The spectral profiles reveal multiple kinematic velocity components that trace different physical entities as well as their distinctive spatial distributions, suggesting that the emission from each COM species can come from different regions. We derive their physical conditions, finding that these COMs trace a complex structure in the protobinary system SVS13A. Our main conclusions are summarized as follows:

1. Toward the protobinary system SVS13A, we find that for a given COM species, the spatial distributions of different transitions show similar structures based on the uv-space Gaussian fitting at different velocities. However, different COMs do not trace the same kinematic components. This necessitates a caveat when discussing the abundance ratios and chemical properties of COMs without kinematically resolving the systems. The measurement of relative COM abundances requires high-spectral-resolution (as well as high-angular-resolution) observations.
2. By covering numerous transitions with high spectral resolution, we decomposed the emission of each COM into several kinematic components. We suggest that the traditional rotational diagram or one-component fitting can underestimate the total amount of molecules. We find that each COM can contain multiple velocity components within tens of astronomical units of the hot corino, which trace different physical conditions.

3. We find that the COM emission from SVS13A is associated with an inhomogeneous complex structure. The small source sizes show that the emission likely does not arise from outflow cavity walls. It is unlikely that this complex structure is caused only by heating from the central protostar. We conclude that the COM emission most likely comes from shocked gas at disk scales. The shocked gas may be induced by the large-scale streamer (Hsieh et al. 2023), which may be infalling directly onto the disk and producing inhomogeneous shocked regions.

Our results suggest that different COMs can trace very different kinematic components in a system. This means we have to be careful when comparing abundances before resolving the system. The emission of an individual COM can be associated with multiple components. This suggests that COM emission is influenced by localized shock activities instead of only the protostellar heating.

Acknowledgements. We are grateful for the anonymous referee for the thorough and insightful comments that helped to improve this paper significantly. T.-H.H., J.E.P., P.C., M.T.V, C.G., and M.J.M. acknowledge the support by the Max Planck Society. The authors thank Eleonora Bianchi Valerio Lattanzi, Silvia Spezzano, and Christian Endres for the chemical modeling and CDMS. D.S.-C. is supported by an NSF Astronomy and Astrophysics Postdoctoral Fellowship under award AST-2102405. I.J-.S acknowledges funding from grants No. PID2019-105552RB-C41 and PID2022-136814NB-I00 funded by MICIU/AEI/10.13039/501100011033 and by "ERDF/EU". This work is based on observations carried out under project number L19MB with the IRAM NOEMA Interferometer. IRAM is supported by INSU/CNRS (France), MPG (Germany) and IGN (Spain). This paper makes use of the following ALMA data: ADS/JAO.ALMA#2013.1.00031.S and 2016.1.01305. ALMA is a partnership of ESO (representing its member states), NSF (USA) and NINS (Japan), together with NRC (Canada), MOST and ASIAA (Taiwan), and KASI (Republic of Korea), in cooperation with the Republic of Chile. The Joint ALMA Observatory is operated by ESO, AUI/NRAO and NAOJ. S.M. is supported by a Royal Society University Research Fellowship (URF-R1-221669). D.S. and Th.H. acknowledge support from the European Research Council under the Horizon 2020 Framework Program via the ERC Advanced Grant Origins 83 24 28. A.F. thanks the Spanish MICIN for funding support from PID2019-106235GB-I00 and the European Research Council (ERC) for funding under the Advanced Grant project SUL4LIFE, grant agreement No101096293.

Software: Numpy (Van Der Walt et al. 2011), Scipy (Virtanen et al. 2020), APLpy (Robitaille & Bressert 2012), Matplotlib (Hunter 2007), Astropy (Astropy Collaboration 2013), CASA (McMullin et al. 2007).

References

Alves, F. O., Cleeves, L. I., Girart, J. M., et al. 2020, ApJ, 904, L6
Anglada, G., Rodríguez, L. F., Osorio, M., et al. 2004, ApJ, 605, L137
Arce, H. G., Santiago-García, J., Jørgensen, J. K., et al. 2008, ApJ, 681, L21
Astropy Collaboration (Robitaille, T. P., et al.) 2013, A&A, 558, A33
Bacmann, A., Taquet, V., Faure, A., et al. 2012, A&A, 541, L12
Belloche, A., Maury, A. J., Maret, S., et al. 2020, A&A, 635, A198
Bianchi, E., Codella, C., Ceccarelli, C., et al. 2017, MNRAS, 467, 3011
Bianchi, E., Codella, C., Ceccarelli, C., et al. 2019, MNRAS, 483, 1850
Bianchi, E., Ceccarelli, C., Codella, C., et al. 2022a, A&A, 662, A103
Bianchi, E., López-Sepulcre, A., Ceccarelli, C., et al. 2022b, ApJ, 928, L3
Blake, G. A., Sutton, E. C., Masson, C. R., et al. 1987, ApJ, 315, 621
Bottinelli, S., Ceccarelli, C., Lefloch, B., et al. 2004, ApJ, 615, 354
Bottinelli, S., Ceccarelli, C., Williams, J. P., et al. 2007, A&A, 463, 601
Bouvier, M., López-Sepulcre, A., Ceccarelli, C., et al. 2021, A&A, 653, A117
Butler, R. A. H., De Lucia, F. C., Petkie, D. T., et al. 2001, ApJS, 134, 319
Cabedo, V., Maury, A., Girart, J. M., et al. 2021, A&A, 653, A166
Calcutt, H., Jørgensen, J. K., Müller, H. S. P., et al. 2018, A&A, 616, A90
Caselli, P., & Ceccarelli, C. 2012, A&A Rev., 20, 56
Cazaux, S., Tielens, A. G. G. M., Ceccarelli, C., et al. 2003, ApJ, 593, L51
Ceccarelli, C., Caselli, P., Fontani, F., et al. 2017, ApJ, 850, 176
Ceccarelli, C., Codella, C., Balucani, N., et al. 2022, arXiv e-prints [arXiv:2206.13270]
Choudhury, S., Pineda, J. E., Caselli, P., et al. 2020, A&A, 640, L6
Christen, D., & Müller, H. S. P. 2003, Phys. Chem. Chem. Phys., 5, 3600
Christen, D., Coudert, L. H., Larsson, J. A., et al. 2001, J. Mol. Spectrosc., 205, 185
Codella, C., Bianchi, E., Tabone, B., et al. 2018, A&A, 617, A10
Codella, C., Bianchi, E., Podio, L., et al. 2021, A&A, 654, A52
Coletta, A., Fontani, F., Rivilla, V. M., et al. 2020, A&A, 641, A54
Csengeri, T., Bontemps, S., Wyrowski, F., et al. 2018, A&A, 617, A89
Csengeri, T., Belloche, A., Bontemps, S., et al. 2019, A&A, 632, A57
Diaz-Rodriguez, A. K., Anglada, G., Blázquez-Calero, G., et al. 2022, ApJ, 930, 91
Drozdovskaya, M. N., Walsh, C., Visser, R., et al. 2015, MNRAS, 451, 3836
Endres, C. P., Drouin, B. J., Pearson, J. C., et al. 2009, A&A, 504, 635
Endres, C. P., Schlemmer, S., Schilke, P., et al. 2016, J. Mol. Spectrosc., 327, 95
Foreman-Mackey, D., Hogg, D. W., Lang, D., et al. 2013, PASP, 125, 306
Garufi, A., Dominik, C., Ginski, C., et al. 2022, A&A, 658, A137
Gieser, C., Beuther, H., Semenov, D., et al. 2023, A&A, 674, A160
Ginski, C., Facchini, S., Huang, J., et al. 2021, ApJ, 908, L25
Goodman, J., & Weare, J. 2010, Commun. Appl. Math. Comput. Sci., 5, 65
Harsono, D., Visser, R., Bruderer, S., et al. 2013, A&A, 555, A45
Herbst, E., & van Dishoeck, E. F. 2009, ARA&A, 47, 427
Hogg, D. W., & Foreman-Mackey, D. 2018, ApJS, 236, 11
Hsieh, T.-H., Murillo, N. M., Belloche, A., et al. 2019, ApJ, 884, 149
Hsieh, T.-H., Segura-Cox, D. M., Pineda, J. E., et al. 2023, A&A, 669, A137
Hunter, J. D. 2007, Comput. Sci. Eng., 9, 90
Ilyushin, V., Kryvda, A., & Alekseev, E. 2009, J. Mol. Spectrosc., 255, 32
Jørgensen, J. K., Hogerheijde, M. R., Blake, G. A., et al. 2004, A&A, 415, 1021
Jørgensen, J. K., van der Wiel, M. H. D., Coutens, A., et al. 2016, A&A, 595, A117
Jørgensen, J. K., Müller, H. S. P., Calcutt, H., et al. 2018, A&A, 620, A170
Jørgensen, J. K., Belloche, A., & Garrod, R. T. 2020, ARA&A, 58, 727
Kleiner, I., Lovas, F. J., & Godefroid, M. 1996, J. Phys. Chem. Ref. Data, 25, 1113
Lefèvre, C., Cabrit, S., Maury, A. J., et al. 2017, A&A, 604, L1
Lefloch, B., Bachiller, R., Ceccarelli, C., et al. 2018, MNRAS, 477, 4792
Maureira, M. J., Pineda, J. E., Segura-Cox, D. M., et al. 2020, ApJ, 897, 59
Maureira, M. J., Gong, M., Pineda, J. E., et al. 2022, ApJ, 941, L23
McMullin, J. P., Waters, B., Schiebel, D., et al. 2007, Astronomical Data Analysis Software and Systems XVI, 376, 127
Möller, T., Endres, C., & Schilke, P. 2017, A&A, 598, A7
Müller, H. S. P., Schlöder, F., Stutzki, J., et al. 2005, J. Mol. Struc., 742, 215
Müller, H. S. P., Belloche, A., Xu, L.-H., et al. 2016, A&A, 587, A92
Murillo, N. M., van Dishoeck, E. F., Hacar, A., et al. 2022, A&A, 658, A53
Ortiz-León, G. N., Loinard, L., Dzib, S. A., et al. 2018, ApJ, 869, L33
Oya, Y., & Yamamoto, S. 2020, ApJ, 904, 185
Oya, Y., Sakai, N., López-Sepulcre, A., et al. 2016, ApJ, 824, 88
Palau, A., Walsh, C., Sánchez-Monge, Á., et al. 2017, MNRAS, 467, 2723
Pearson, J. C., Brauer, C. S., & Drouin, B. J. 2008, J. Mol. Spectrosc., 251, 394
Pineda, J. E., Maury, A. J., Fuller, G. A., et al. 2012, A&A, 544, L7
Pineda, J. E., Segura-Cox, D., Caselli, P., et al. 2020, Nat. Astron., 4, 1158
Pineda, J. E., Arzoumanian, D., André, P., et al. 2023, ASP Conf. Ser., 534, 233
Robitaille, T., & Bressert, E. 2012, Astrophysics Source Code Library [record ascl:1208.017]
Sargent, A. I., & Beckwith, S. 1987, ApJ, 323, 294
Segura-Cox, D. M., Looney, L. W., Tobin, J. J., et al. 2018, ApJ, 866, 161
Spezzano, S., Bizzocchi, L., Caselli, P., et al. 2016, A&A, 592, L11
Sugimura, M., Yamaguchi, T., Sakai, T., et al. 2011, PASJ, 63, 459
Tafalla, M., Santiago-García, J., Myers, P. C., et al. 2006, A&A, 455, 577
Thieme, T. J., Lai, S.-P., Lin, S.-J., et al. 2022, ApJ, 925, 32
Tobin, J. J., Looney, L. W., Li, Z.-Y., et al. 2016, ApJ, 818, 73
Tobin, J. J., Looney, L. W., Li, Z.-Y., et al. 2018, ApJ, 867, 43
Tychoniec, Ł., Manara, C. F., Rosotti, G. P., et al. 2020, A&A, 640, A19
Valdivia-Mena, M. T., Pineda, J. E., Segura-Cox, D. M., et al. 2022, A&A, 667, A12 (Paper I)
Van Der Walt, S., Colbert, S. C., & Varoquaux, G. 2011, Comput. Sci. Eng., 13, 22
van Dishoeck, E. F., Blake, G. A., Jansen, D. J., et al. 1995, ApJ, 447, 760
van Dishoeck, E. F. 2014, Faraday Discuss., 168, 9
van Gelder, M. L., Tabone, B., van Dishoeck, E. F., et al. 2021, A&A, 653, A159
Vastel, C., Alves, F., Ceccarelli, C., et al. 2022, A&A, 664, A171
Virtanen, P., Gommers, R., Oliphant, T. E., et al. 2020, Nat. Meth., 17, 261
Xu, L.-H., Fisher, J., Lees, R. M., et al. 2008, J. Mol. Spectrosc., 251, 305
Yang, Y.-L., Sakai, N., Zhang, Y., et al. 2021, ApJ, 910, 20

Appendix A: Line stacking

To unveil the complexity of the line profiles, we stacked spectra from manually selected transitions using SciPy and NumPy; these transitions were selected to have similar line profiles and to not be contaminated by other lines. Figure A.1 shows the individual line profiles in comparison to the stacked line profiles presented in Fig. 3. These transitions are selected as they share similar normalized spectrum profiles; we compared the averaged profiles with the candidate transition to see if they look similar. If yes, the transition was added for stacking. In the off-peak velocities, the continuum-subtracted fluxes sometimes do not reach zero since they can still be affected by contamination from other molecular line transitions.

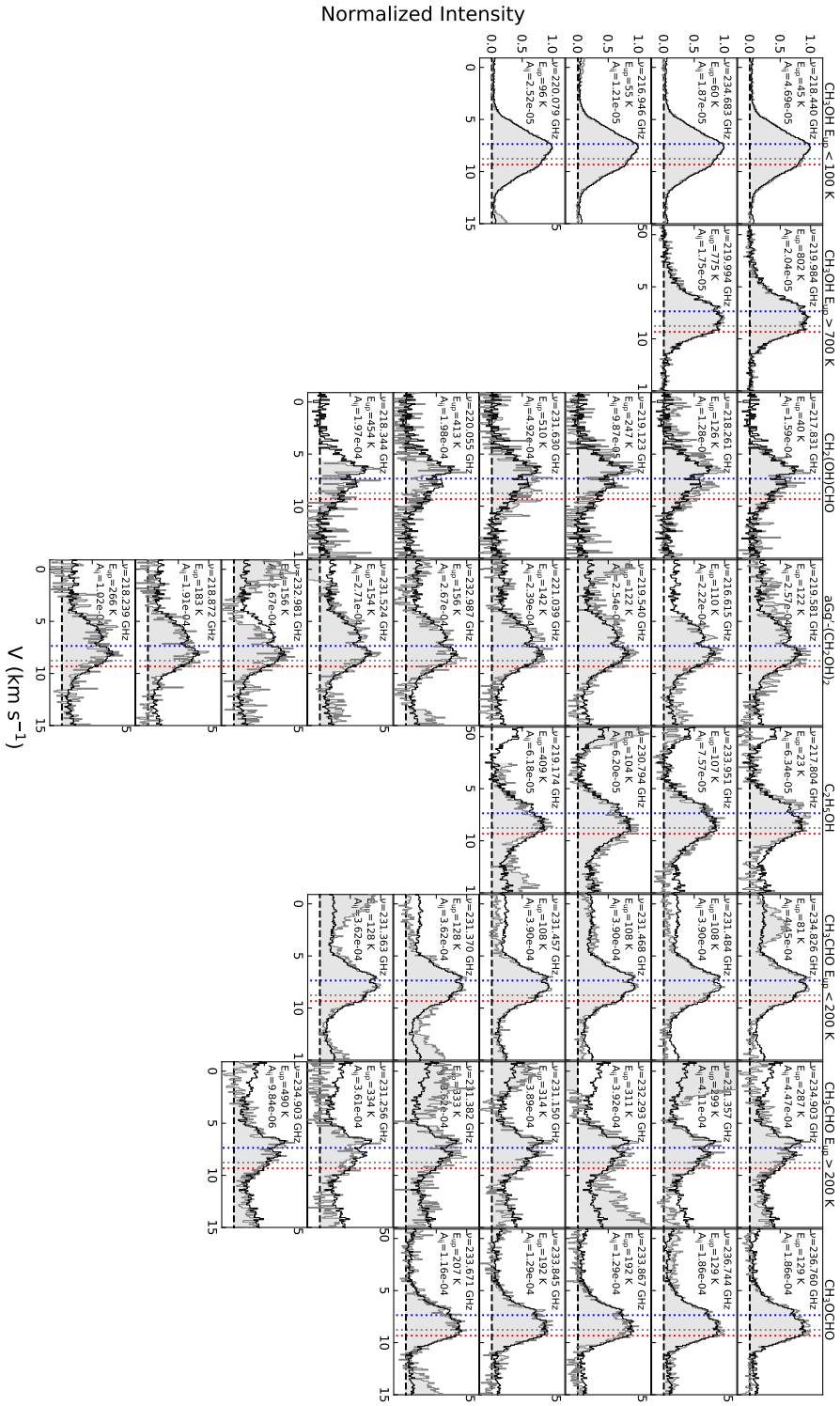

Fig. A.1. All spectral profiles used for the line stacking. Each column shows all the transitions of a particular species used in the line stacking, as gray-filled histograms. The black histograms represent the resulting stacked spectrum of each molecule, for comparison.

Appendix B: Line fitting

Figures B.1 to B.6 show the best-fit profiles of the one-component fitting for all transitions in use (see Sect. 4.1). Figure B.7 shows the relative intensity as a function of the upper energy level for those transitions involved in the fitting; more importantly, the colors represent the optical depths from the single-component fitting. The transitions used are listed in Tables B.1 to B.6; they are summarized in the CDMS, with individual molecule originally measured by: CH_3OH (Xu et al. 2008), aGg'-$(CH_2OH)_2$ (Christen & Müller 2003), C_2H_5OH (Pearson et al. 2008; Müller et al. 2016), $CH_2(OH)CHO$ (Butler et al. 2001), CH_3CHO (Kleiner et al. 1996), CH_3OCHO (Ilyushin et al. 2009), and CH_3OCH_3 (Endres et al. 2009). Optically thick lines are required in order to derive the source size (see Sect. 4.1). On the other hand, a broad range of E_{up} will constrain the physical conditions and perhaps identify different temperature components. Also, a large number of transitions in use is crucial, especially for multicomponent fitting.

For each COM, we started by fitting one component and added an extra component with each iteration of the fit. For each iteration, χ^2 and ΔAIC were calculated to help evaluate if adding one more component would improve the fit (Table 3). We stopped adding additional components when the χ^2 did not significantly improve relative to the previous iteration and/or the fitting found an unreasonable component. Take C_2H_5OH as an example. We stopped adding a new component at the two-component model because the third component contributes emission at about the noise level with an extreme high optical depth (9×10^{22} cm^{-2}). Whether this component is real or not is difficult to judge with the current dataset and severe line contamination in this source. Therefore, we adopted the two-component model for C_2H_5OH. After the numbers of components were determined, we conducted MCMC fitting using `emcee` as well as one-component fitting.

Table B.1. Transitions for the fitting: CH_3OH.

Rest frequency (MHz)	Transition	E_{up} (K)	A_{ij} (s^{-1})	upper state degeneracy	$\tau_{1comp.}$	Gau. fitting/stacked	uv-space center	S/N
215418.3060	14_9-15_{10}	1295.6	3.29e-05	29	0.018	-	-	2.2
216945.6000	$5_{1,4}-4_{2,3}$	55.9	1.21e-05	44	2.247	yes	yes	58.5
218440.0500	$4_{2,3}-3_{1,2}$	45.5	4.69e-05	36	7.334	yes	yes	64.8
219983.6610	$25_{3,..}-24_{4,..}$	802.2	2.04e-05	200	0.641	yes	yes	24.0
219993.6380	$23_{5,..}-22_{6,..}$	775.9	1.75e-05	190	0.585	yes	yes	22.4
220078.5190	$8_{0,8}-7_{1,6}$	96.6	2.52e-05	68	5.862	yes	yes	57.8
230817.6590	$18_{6,..}-18_{7,..}$	987.6	3.13e-06	150	0.030	-	-	4.5
230820.1620	$30_{9,}-31_{11,}$	1757.7	5.29e-08	240	0.000	-	-	blend
230820.1620	$30_{9,}-31_{11,}$	1757.7	5.29e-08	240	0.000	-	-	blend
234683.3900	$4_{2,3}-5_{1,4}$	60.9	1.87e-05	36	2.379	yes	-	57.8

Notes. The transitions used for LTE model fitting. Column 1-5: The transition information obtained from CDMS using the XCLASS task `ListDatabase`. Column 6: Optical depths derived from the one-component LTE model fitting, which are also shown in Fig. B.7. Column 7: The transitions that are used in the Gaussian fitting (Fig. 4) and the stacked process (Fig. A.1). Column 8: The transitions used for 2D Gaussian fitting in the uv-space for the emitting centers in Fig. 5. Column 9: The signal to noise ratio obtained given the peak pixel value at the resolution of ∼ 0.08 km s^{-1}. "blend" indicates that the transition is blended with nearby transitions of the same molecule, for which we only list one S/N for the group (see Fig. B.1).

Table B.2. Transitions for the fitting: aGg'-$(CH_2OH)_2$.

Rest frequency (MHz)	Transition	E_{up} (K)	A_{ij} (s^{-1})	upper state degeneracy	$\tau_{1comp.}$	Gau. fitting/stacked	uv-space center	S/N
215238.6439	$24_{4,20}-23_{5,19}$	159.4	2.26e-05	440	0.184	-	-	3.6
215437.2856	$39_{4,36}-39_{3,37}$	384.0	1.38e-05	550	0.055	-	-	2.6
216614.9524	$20_{3,17}-19_{3,16}$	110.8	2.22e-04	370	1.835	yes	yes	9.5
217089.5511	$36_{2,34}-36_{2,35}$	321.3	4.14e-06	660	0.025	-	-	3.0
217090.7383	$36_{3,34}-36_{1,35}$	321.3	4.15e-06	510	0.020	-	-	blend
217392.5992	$30_{11,20}-30_{10,20}$	288.6	5.20e-06	430	0.024	-	-	1.5
218238.2595	$47_{6,41}-47_{5,42}$	580.6	2.45e-05	660	0.051	-	-	blend
218238.9880	$22_{17,6}-21_{17,5}$	266.2	1.02e-04	400	0.470	yes	yes	6.7
218238.9880	$22_{17,5}-21_{17,4}$	266.2	1.02e-04	320	0.376	yes	yes	6.7
218240.7716	$33_{7,26}-32_{8,24}$	303.4	3.97e-06	600	0.024	-	-	blend
218271.7930	$50_{7,43}-50_{6,44}$	661.7	2.27e-05	710	0.036	-	-	2.5
218304.6705	$22_{16,6}-21_{16,5}$	250.0	1.19e-04	320	0.471	-	-	6.8
218304.6705	$22_{16,7}-21_{16,6}$	250.0	1.19e-04	400	0.588	-	-	6.8
218872.1123	$22_{11,12}-21_{11,11}$	183.8	1.91e-04	400	1.235	yes	yes	8.8
218872.1125	$22_{11,11}-21_{11,10}$	183.8	1.91e-04	320	0.988	-	-	blend
219573.0047	$45_{12,33}-44_{13,32}$	581.1	5.98e-06	820	0.015	-	-	2.1
219573.2390	$45_{12,33}-44_{13,32}$	581.4	8.05e-06	640	0.016	-	-	blend
220006.7517	$50_{8,43}-50_{7,44}$	662.1	2.28e-05	710	0.035	-	-	2.2
220006.9692	$37_{8,30}-36_{9,27}$	379.8	6.35e-06	680	0.031	-	-	blend
220092.8238	$24_{11,14}-24_{10,14}$	207.2	5.15e-06	340	0.025	-	-	blend
220092.9046	$24_{11,13}-24_{10,15}$	207.2	5.15e-06	440	0.033	-	-	2.4
220649.9710	$22_{11,12}-22_{10,12}$	184.1	5.01e-06	320	0.025	-	-	blend
220649.9844	$22_{11,11}-22_{10,13}$	184.1	5.01e-06	400	0.032	-	-	1.9
220719.4817	$22_{3,20}-21_{2,19}$	127.8	5.77e-05	320	0.370	-	-	3.7
221038.7997	$22_{6,17}-21_{6,16}$	142.6	2.39e-04	400	1.800	yes	yes	8.5
221081.5463	$20_{11,10}-20_{10,10}$	163.0	4.79e-06	290	0.024	-	-	blend
221081.5482	$20_{11,9}-20_{10,11}$	163.0	4.79e-06	370	0.031	-	-	2.6
221950.7013	$12_{11,2}-12_{10,2}$	98.1	1.98e-06	180	0.008	-	-	2.4
221950.7013	$12_{11,1}-12_{10,3}$	98.1	1.98e-06	220	0.010	-	-	2.4
231053.5229	$25_{4,21}-24_{5,20}$	171.7	7.64e-06	460	0.054	-	-	1.9
231127.4008	$23_{7,16}-22_{7,15}$	160.2	2.72e-04	420	1.829	-	-	8.6
231303.7540	$33_{12,21}-33_{11,22}$	347.0	3.47e-05	470	0.120	-	-	blend
231306.4079	$33_{12,22}-33_{11,23}$	347.0	3.48e-05	600	0.153	-	-	3.8
231524.0331	$23_{6,18}-22_{6,17}$	154.1	2.71e-04	330	1.465	yes	yes	9.1
231639.2407	$13_{5,9}-12_{4,9}$	57.4	8.34e-06	240	0.049	-	-	2.5
232257.7074	$22_{19,3}-21_{19,2}$	301.8	7.74e-05	400	0.273	-	-	4.7
232257.7074	$22_{19,4}-21_{19,3}$	301.8	7.74e-05	320	0.218	-	-	4.7
232981.0084	$22_{8,15}-21_{8,14}$	156.3	2.67e-04	320	1.367	yes	yes	7.4
232987.3530	$22_{8,14}-21_{8,13}$	156.3	2.67e-04	400	1.708	yes	yes	7.7
233664.3187	$22_{7,15}-21_{7,14}$	149.1	2.79e-04	400	1.828	-	-	8.5
234791.8788	$22_{12,10}-22_{11,11}$	195.4	2.92e-05	400	0.157	-	-	6.2
234791.8791	$22_{12,11}-22_{11,12}$	195.4	2.92e-05	320	0.125	-	-	blend
234923.7899	$21_{12,9}-21_{11,10}$	184.6	2.82e-05	300	0.118	-	-	blend
234923.7900	$21_{12,10}-21_{11,11}$	184.6	2.82e-05	390	0.154	-	-	3.6
235169.3027	$18_{12,7}-18_{11,8}$	154.7	2.23e-05	330	0.116	-	-	blend
235169.3027	$18_{12,6}-18_{11,7}$	154.7	2.23e-05	260	0.092	-	-	blend
235170.4758	$51_{13,39}-51_{12,40}$	737.1	4.73e-05	930	0.062	-	-	blend
235170.5737	$23_{3,21}-22_{3,20}$	138.7	2.91e-04	420	2.063	-	-	8.0
235170.6954	$39_{1,38}-39_{1,39}$	362.6	2.56e-06	710	0.012	-	-	blend
235170.7008	$39_{2,38}-39_{0,39}$	362.6	2.56e-06	550	0.009	-	-	blend
237078.6119	$39_{8,32}-38_{9,29}$	418.2	8.11e-06	710	0.030	-	-	2.3

Notes. Same as Table B.1 but for aGg'-$(CH_2OH)_2$ and corresponding to Fig. B.2.

Table B.3. Transitions for the fitting: C_2H_5OH.

Rest frequency (MHz)	Transition	E_{up} (K)	A_{ij} (s^{-1})	upper state degeneracy	$\tau_{1comp.}$	Gau. fitting/stacked	uv-space center	S/N
216521.6912	$8_{4,4}-7_{3,4}$	106.3	3.65e-05	17	0.225	-	-	5.9
217254.2631	$33_{7,26}-33_{9,25}$	583.9	7.66e-06	67	0.001	-	-	2.3
217803.7431	$5_{3,3}-4_{2,2}$	23.9	6.34e-05	11	0.582	yes	yes	9.2
219523.3306	$37_{7,30}-37_{6,32}$	702.7	2.72e-05	75	0.002	-	-	1.4
219966.3193	$33_{7,26}-33_{6,28}$	583.9	2.16e-05	67	0.004	-	-	2.7
220627.5393	$38_{7,31}-38_{6,33}$	734.5	2.69e-05	77	0.001	-	-	2.2
220770.1935	$68_{1,67}-68_{3,66}$	1925.2	1.32e-05	140	0.000	-	-	2.8
220770.2093	$68_{2,67}-68_{2,66}$	1925.2	1.32e-05	140	0.000	-	-	blend
230793.7639	$6_{5,1}-5_{4,1}$	104.8	6.20e-05	13	0.263	yes	-	11.6
230793.8643	$6_{5,2}-5_{4,2}$	104.8	6.20e-05	13	0.263	yes	-	blend
233951.2316	$13_{5,9}-13_{4,10}$	107.9	7.57e-05	27	0.628	yes	yes	12.2
234758.8524	$6_{3,4}-5_{2,3}$	28.9	7.09e-05	13	0.632	-	-	11.8
234871.3761	$48_{13,36}-47_{14,34}$	1245.2	9.78e-06	97	0.000	-	-	blend
234871.3864	$48_{13,35}-47_{14,33}$	1245.2	9.78e-06	97	0.000	-	-	blend
234873.8737	$9_{5,5}-9_{4,6}$	69.2	6.54e-05	19	0.563	-	-	8.5
234882.5377	$14_{2,12}-13_{3,10}$	155.2	3.64e-05	29	0.198	-	-	5.6
235129.2333	$31_{16,16}-32_{15,17}$	786.9	1.89e-07	63	0.000	-	-	blend
235129.2333	$31_{16,15}-32_{15,18}$	786.9	1.89e-07	63	0.000	-	-	blend
235131.4085	$6_{5,1}-6_{4,2}$	49.0	4.36e-05	13	0.315	-	-	11.2
235132.1549	$6_{5,2}-6_{4,3}$	49.0	4.36e-05	13	0.315	-	-	blend
235158.3101	$35_{4,31}-34_{9,25}$	613.4	1.74e-07	71	0.000	-	-	blend
235158.4949	$14_{0,14}-13_{1,12}$	146.4	1.12e-04	29	0.667	-	-	11.1
235983.3336	$41_{9,33}-40_{10,30}$	877.2	1.07e-06	83	0.000	-	-	blend
235983.3517	$14_{1,14}-13_{0,13}$	85.6	1.28e-04	29	1.409	yes	yes	17.5
237059.8552	$5_{3,2}-5_{0,5}$	23.9	2.25e-07	11	0.002	-	-	2.5

Notes. Same as Table B.1 but for C_2H_5OH and corresponding to Fig. B.3.

Table B.4. Transitions for the fitting: $CH_2(OH)CHO$.

Rest frequency (MHz)	Transition	E_{up} (K)	A_{ij} (s^{-1})	upper state degeneracy	$\tau_{1comp.}$	Gau. fitting/stacked	uv-space center	S/N
216162.1513	$18_{9,}-18_{8,}$	518.6	1.93e-04	37	0.023	-	-	3.0
216262.6061	$20_{3,}-19_{4,}$	406.4	1.66e-04	41	0.045	-	-	2.9
217830.6936	$9_{5,4}-8_{4,5}$	40.2	1.59e-04	19	0.220	yes	yes	9.1
217832.2544	$67_{18,}-68_{15,}$	1909.6	1.48e-06	140	0.000	-	-	blend
217923.6615	$12_{9,}-12_{8,}$	467.2	1.31e-04	25	0.014	-	-	blend
217923.6655	$12_{9,}-12_{8,}$	467.2	1.31e-04	25	0.014	-	-	3.3
218260.5472	$20_{3,17}-19_{4,16}$	126.1	1.28e-04	41	0.216	yes	yes	7.8
218344.0177	$37_{10,28}-37_{9,29}$	454.9	1.97e-04	75	0.070	yes	yes	3.8
219122.8509	$29_{3,26}-29_{2,27}$	247.8	9.87e-05	59	0.107	yes	yes	5.0
219519.6879	$19_{16,4}-18_{16,3}$	260.9	1.20e-06	39	0.001	-	-	2.7
219519.6879	$19_{16,3}-18_{16,2}$	260.9	1.20e-06	39	0.001	-	-	2.7
220055.1566	$35_{10,26}-35_{9,27}$	413.5	1.98e-04	71	0.086	yes	yes	5.6
220420.3366	$19_{10,10}-18_{10,9}$	166.3	3.02e-06	39	0.004	-	-	2.2
220420.3451	$19_{10,9}-18_{10,8}$	166.3	3.02e-06	39	0.004	-	-	blend
231206.1660	$20_{15,6}-19_{15,5}$	253.2	2.11e-06	41	0.001	-	-	2.5
231206.1660	$20_{15,5}-19_{15,4}$	253.2	2.11e-06	41	0.001	-	-	2.5
231624.9077	$38_{6,}-38_{5,}$	892.9	2.53e-04	77	0.005	-	-	blend
231626.7190	$20_{12,8}-19_{12,7}$	204.0	3.10e-06	41	0.003	-	-	5.1
231626.7190	$20_{12,9}-19_{12,8}$	204.0	3.10e-06	41	0.003	-	-	5.1
231627.9025	$21_{2,}-20_{2,}$	411.6	9.83e-07	43	0.000	-	-	blend
231629.5555	$44_{11,}-45_{8,}$	1001.6	1.15e-06	89	0.000	-	-	blend
231629.6217	$23_{0,}-22_{1,}$	510.1	4.92e-04	47	0.068	-	-	6.3
231629.8905	$23_{1,}-22_{1,}$	510.1	1.01e-06	47	0.000	-	-	blend
231630.0690	$23_{0,}-22_{0,}$	510.1	1.01e-06	47	0.000	-	-	blend
231630.2222	$23_{1,}-22_{0,}$	510.1	4.92e-04	47	0.068	yes	yes	blend
232955.0612	$8_{6,3}-7_{5,2}$	416.3	3.55e-04	17	0.032	-	-	blend
232956.1338	$8_{6,2}-7_{5,3}$	416.3	3.55e-04	17	0.032	-	-	3.7
233835.9409	$69_{14,}-69_{14,}$	1928.6	3.59e-08	140	0.000	-	-	blend
233837.7340	$39_{10,29}-38_{11,28}$	499.3	4.90e-05	79	0.012	-	-	1.4
233840.2668	$62_{38,}-63_{37,}$	2335.9	2.39e-05	120	0.000	-	-	blend
233840.7525	$31_{24,}-32_{23,}$	1077.3	1.05e-05	63	0.000	-	-	blend
233903.4944	$12_{4,}-11_{3,}$	504.7	1.47e-04	25	0.011	-	-	2.2
233904.5100	$69_{17,}-70_{14,}$	1896.0	2.10e-06	140	0.000	-	-	blend
233904.5390	$20_{3,}-19_{3,}$	406.4	1.00e-06	41	0.000	-	-	blend
234298.4439	$29_{3,}-29_{2,}$	517.5	1.12e-04	59	0.018	-	-	3.2
234298.7988	$29_{3,}-29_{1,}$	517.5	2.17e-08	59	0.000	-	-	blend
234808.3442	$26_{10,}-26_{9,}$	536.3	2.85e-04	53	0.036	-	-	4.7
234939.5820	$35_{6,30}-35_{5,31}$	373.6	1.69e-04	71	0.084	-	-	4.4
236068.8441	$27_{10,}-27_{9,}$	645.0	2.95e-04	55	0.019	-	-	1.9
236765.8791	$50_{10,41}-49_{11,38}$	778.9	1.82e-05	100	0.001	-	-	blend
236768.5784	$26_{10,}-26_{9,}$	706.4	2.92e-04	53	0.012	-	-	2.6

Notes. Same as Table B.1 but for $CH_2(OH)CHO$ and corresponding to Fig. B.4.

Table B.5. Transitions for the fitting: CH_3CHO.

Rest frequency (MHz)	Transition	E_{up} (K)	A_{ij} (s^{-1})	upper state degeneracy	$\tau_{1comp.}$	Gau. fitting/stacked	uv-space center	S/N
215417.8208	$10_{2,8}-10_{1,10}$	266.3	4.05e-06	42	0.003	-	-	2.2
216294.8253	$11_{1,10}-10_{1,9}$	269.6	3.50e-04	46	0.283	-	-	blend
216513.2543	$11_{9,2}-10_{9,1}$	608.7	1.14e-04	46	0.010	-	-	2.3
216513.2579	$11_{9,3}-10_{9,2}$	608.7	1.14e-04	46	0.010	-	-	blend
216534.3635	$14_{3,11}-14_{2,12}$	117.7	3.45e-05	58	0.093	yes	yes	4.6
216581.9304	$11_{1,10}-10_{1,9}$	64.9	3.55e-04	46	1.064	-	-	blend
216983.0811	$19_{2,17}-19_{1,18}$	573.0	1.27e-05	78	0.002	-	-	blend
217405.0497	$15_{2,14}-15_{0,15}$	119.7	1.85e-06	62	0.005	-	-	2.7
218893.9256	$37_{7,30}-38_{5,33}$	1135.4	1.27e-07	150	0.000	-	-	blend
218894.1368	$31_{4,28}-32_{9,24}$	886.0	1.06e-08	130	0.000	-	-	blend
220058.5907	$19_{1,18}-19_{1,19}$	553.8	1.53e-06	78	0.000	-	-	blend
231114.2208	$9_{3,6}-9_{2,7}$	62.0	2.88e-05	38	0.064	-	-	blend
231116.5868	$12_{8,5}-11_{8,4}$	421.5	2.42e-04	50	0.071	-	-	5.8
231116.5868	$12_{8,4}-11_{8,3}$	421.5	2.42e-04	50	0.071	-	-	5.8
231149.4163	$12_{11,1}-11_{11,0}$	344.6	6.98e-05	50	0.033	-	-	blend
231150.2734	$12_{4,8}-11_{4,7}$	314.3	3.89e-04	50	0.226	-	-	8.6
231212.6277	$12_{10,2}-11_{10,1}$	297.3	1.33e-04	50	0.086	-	-	10.1
231212.6277	$12_{10,3}-11_{10,2}$	297.3	1.33e-04	50	0.086	-	-	10.1
231255.9108	$12_{5,7}-11_{5,6}$	334.4	3.61e-04	50	0.184	yes	yes	8.8
231268.3856	$12_{7,6}-11_{7,5}$	182.5	2.88e-04	50	0.389	-	-	blend
231269.9018	$12_{6,7}-11_{6,6}$	153.4	3.28e-04	50	0.533	-	-	27.4
231269.9031	$12_{6,6}-11_{6,5}$	153.4	3.28e-04	50	0.533	-	-	blend
231270.2061	$15_{4,12}-16_{2,15}$	350.8	1.58e-07	62	0.000	-	-	27.4
231329.6393	$12_{5,8}-11_{5,7}$	128.6	3.62e-04	50	0.689	-	-	27.4
231329.7936	$12_{5,7}-11_{5,6}$	128.6	3.62e-04	50	0.689	-	-	blend
231332.3518	$19_{19,1}-18_{17,2}$	1183.1	1.74e-07	78	0.000	-	-	blend
231357.3496	$12_{3,9}-11_{3,8}$	299.1	4.11e-04	50	0.263	yes	yes	10.3
231363.2836	$12_{5,7}-11_{5,6}$	128.5	3.62e-04	50	0.689	-	-	20.1
231369.8292	$12_{5,8}-11_{5,7}$	128.5	3.62e-04	50	0.689	yes	-	19.2
231382.1065	$12_{5,8}-11_{5,7}$	333.6	3.62e-04	50	0.185	yes	-	7.1
231427.8171	$4_{4,0}-5_{3,2}$	45.4	1.85e-06	18	0.002	-	-	2.5
231456.7437	$12_{4,9}-11_{4,8}$	108.4	3.90e-04	50	0.844	yes	yes	21.1
231467.5036	$12_{4,8}-11_{4,7}$	108.4	3.90e-04	50	0.844	yes	-	21.1
231484.3739	$12_{4,8}-11_{4,7}$	108.3	3.90e-04	50	0.844	yes	yes	22.6
232280.2669	$32_{4,28}-31_{5,26}$	733.0	7.02e-06	130	0.001	-	-	blend
232290.3114	$32_{5,27}-31_{6,26}$	926.8	1.23e-08	130	0.000	-	-	blend
232292.6027	$12_{4,9}-11_{4,8}$	311.8	3.92e-04	50	0.228	yes	yes	8.5
234795.4555	$12_{2,10}-11_{2,9}$	81.9	4.45e-04	50	1.109	-	-	blend
234823.4707	$41_{6,36}-40_{7,33}$	1254.2	1.75e-05	170	0.000	-	-	blend
234825.8718	$12_{2,10}-11_{2,9}$	81.8	4.45e-04	50	1.110	yes	yes	22.2
234902.0234	$19_{7,13}-20_{6,14}$	490.8	9.84e-06	78	0.003	-	-	blend
234902.9702	$12_{2,10}-11_{2,9}$	287.2	4.47e-04	50	0.299	-	-	10.5
234903.0341	$19_{7,12}-20_{6,15}$	490.8	9.84e-06	78	0.003	-	-	blend
234904.3343	$17_{4,14}-18_{2,17}$	177.7	6.30e-08	70	0.000	-	-	10.5
236065.5230	$7_{2,6}-6_{1,5}$	238.5	3.18e-06	30	0.002	-	-	blend
236068.6485	$28_{9,20}-29_{8,21}$	557.9	1.12e-05	110	0.003	-	-	1.9
236068.7156	$28_{9,19}-29_{8,22}$	557.9	1.12e-05	110	0.003	-	-	blend
236071.8983	$1_{1,0}-0_{0,0}$	398.5	3.65e-05	6	0.001	-	-	2.4
236527.7307	$4_{3,1}-4_{2,3}$	29.6	1.04e-07	18	0.000	-	-	blend
237040.6540	$35_{4,31}-35_{3,32}$	623.6	6.83e-05	140	0.015	-	-	2.6

Notes. Same as Table B.1 but for CH_3CHO and corresponding to Fig. B.5.

Table B.6. Transitions for the fitting: CH_3OCHO.

Rest frequency (MHz)	Transition	E_{up} (K)	A_{ij} (s^{-1})	upper state degeneracy	$\tau_{1comp.}$	Gau. fitting/stacked	uv-space center	S/N
215420.8580	$50_{10,40}-50_{9,41}$	838.6	1.72e-05	200	0.004	-	-	1.6
216109.7800	$19_{2,18}-18_{2,17}$	109.3	1.49e-04	78	1.843	-	-	blend
216114.9599	$29_{9,20}-29_{8,21}$	312.0	1.51e-05	120	0.071	-	-	blend
216115.5720	$19_{2,18}-18_{2,17}$	109.3	1.49e-04	78	1.843	-	-	blend
216118.1536	$33_{5,28}-33_{5,29}$	542.5	5.25e-06	130	0.005	-	-	blend
216282.5915	$39_{10,30}-38_{11,28}$	715.3	2.69e-06	160	0.001	-	-	1.7
216518.4180	$34_{9,26}-34_{8,27}$	408.1	1.61e-05	140	0.045	-	-	3.6
216588.6310	$33_{9,25}-33_{8,26}$	387.7	1.60e-05	130	0.048	-	-	2.6
216958.8340	$17_{3,14}-16_{3,13}$	286.2	1.48e-04	70	0.484	-	-	blend
216962.9890	$20_{0,20}-19_{1,19}$	111.5	2.45e-05	82	0.312	-	-	blend
216964.1571	$20_{0,20}-19_{1,19}$	111.5	2.44e-05	82	0.311	-	-	blend
216964.7650	$20_{1,20}-19_{1,19}$	111.5	1.53e-04	82	1.951	-	-	blend
216965.9004	$20_{1,20}-19_{1,19}$	111.5	1.53e-04	82	1.952	-	-	blend
216966.2462	$20_{0,20}-19_{0,19}$	111.5	1.53e-04	82	1.951	-	-	blend
216967.4200	$20_{0,20}-19_{0,19}$	111.5	1.53e-04	82	1.952	-	-	blend
216967.9947	$20_{1,20}-19_{0,19}$	111.5	2.45e-05	82	0.312	-	-	blend
216969.1890	$20_{1,20}-19_{0,19}$	111.5	2.44e-05	82	0.311	-	-	blend
217077.0790	$30_{4,26}-30_{4,27}$	291.5	5.12e-06	120	0.028	-	-	1.5
217204.0112	$34_{7,28}-34_{5,29}$	572.5	4.96e-06	140	0.004	-	-	2.3
217215.8470	$32_{9,24}-32_{8,25}$	367.8	1.59e-05	130	0.055	-	-	3.5
217901.8163	$38_{10,28}-38_{9,29}$	692.5	1.45e-05	150	0.006	-	-	2.4
218297.8900	$17_{3,14}-16_{3,13}$	99.7	1.51e-04	70	1.758	-	-	blend
219153.3301	$10_{4,6}-9_{3,6}$	230.5	8.19e-06	42	0.023	-	-	5.1
219154.5340	$18_{11,7}-17_{11,6}$	369.0	9.94e-05	74	0.190	-	-	blend
219566.2450	$18_{15,3}-17_{15,2}$	438.1	4.89e-05	74	0.058	-	-	blend
219566.2450	$18_{15,4}-17_{15,3}$	438.1	4.89e-05	74	0.058	-	-	blend
219568.4800	$18_{14,5}-17_{14,4}$	418.7	6.32e-05	74	0.085	-	-	6.1
219568.4800	$18_{14,4}-17_{14,3}$	418.7	6.32e-05	74	0.085	-	-	6.1
219571.1980	$18_{16,3}-17_{16,2}$	458.9	3.36e-05	74	0.034	-	-	blend
219571.1980	$18_{16,2}-17_{16,1}$	458.9	3.36e-05	74	0.034	-	-	blend
220523.4125	$36_{9,27}-35_{10,26}$	636.4	1.44e-06	150	0.001	-	-	blend
220525.2148	$10_{4,6}-9_{3,7}$	230.8	1.03e-05	42	0.029	-	-	2.4
220671.4458	$29_{9,20}-29_{8,21}$	497.9	1.23e-05	120	0.015	-	-	2.3
221047.7910	$18_{14,4}-17_{14,3}$	230.9	6.45e-05	74	0.314	-	-	blend
221047.7910	$18_{14,5}-17_{14,4}$	230.9	6.45e-05	74	0.314	-	-	blend
221049.9900	$18_{14,4}-17_{14,3}$	230.9	6.45e-05	74	0.314	-	-	blend
221064.4128	$7_{3,5}-6_{0,6}$	22.5	3.18e-07	30	0.003	-	-	blend
221066.9330	$18_{14,5}-17_{14,4}$	230.9	6.45e-05	74	0.314	-	-	blend
221075.9810	$29_{9,21}-29_{8,22}$	312.0	1.61e-05	120	0.073	-	-	blend
221082.0006	$10_{5,5}-10_{3,8}$	49.1	3.43e-07	42	0.003	-	-	blend
221086.1780	$29_{9,21}-29_{8,22}$	312.0	1.61e-05	120	0.073	-	-	3.2
231045.9845	$12_{4,9}-11_{3,8}$	56.8	1.03e-05	50	0.103	-	-	3.9
231047.4058	$36_{25,12}-37_{24,13}$	995.6	9.42e-07	150	0.000	-	-	blend
231047.5117	$36_{25,11}-37_{24,14}$	995.6	9.42e-07	150	0.000	-	-	blend
233669.9773	$38_{9,30}-37_{10,28}$	680.5	1.59e-06	150	0.001	-	-	blend
233670.9800	$19_{12,8}-18_{12,7}$	207.6	1.16e-04	78	0.626	yes	yes	10.7
233845.2330	$19_{11,8}-18_{11,7}$	192.4	1.29e-04	78	0.770	yes	yes	12.0
233854.2860	$19_{11,8}-18_{11,7}$	192.4	1.29e-04	78	0.770	-	-	17.2
233854.2860	$19_{11,9}-18_{11,8}$	192.4	1.29e-04	78	0.770	-	-	17.2
233867.1930	$19_{11,9}-18_{11,8}$	192.4	1.29e-04	78	0.770	yes	yes	12.4
233959.0100	$16_{9,8}-16_{8,9}$	134.0	1.39e-05	66	0.105	-	-	4.4
234674.9700	$19_{9,11}-19_{8,12}$	353.1	1.59e-05	78	0.031	-	-	1.3
234735.6500	$13_{9,5}-13_{8,6}$	107.4	1.13e-05	54	0.084	-	-	blend
234737.4750	$9_{5,5}-8_{4,4}$	43.2	1.70e-05	38	0.138	-	-	7.8
234739.1110	$20_{2,18}-19_{3,17}$	128.0	1.98e-05	82	0.193	-	-	blend
234915.0220	$36_{7,30}-36_{5,31}$	430.1	6.93e-06	150	0.015	-	-	blend
234916.8050	$9_{5,4}-8_{4,5}$	43.2	1.70e-05	38	0.138	-	-	4.9
235122.0070	$10_{9,2}-10_{8,3}$	86.2	6.43e-06	42	0.043	-	-	3.0
235144.4940	$10_{9,1}-10_{8,2}$	86.2	6.42e-06	42	0.043	-	-	3.6
235145.0245	$44_{8,36}-44_{8,37}$	644.6	7.04e-06	180	0.004	-	-	blend

Table B.6. Continued.

Rest frequency (MHz)	Transition	E_{up} (K)	A_{ij} (s^{-1})	upper state degeneracy	$\tau_{1comp.}$	Gau. fitting/stacked	uv-space center	S/N
236108.2250	$21_{1,20}-20_{2,19}$	318.0	2.60e-05	86	0.071	-	-	4.9
236465.2486	$41_{7,34}-41_{6,35}$	739.5	1.85e-05	170	0.005	-	-	1.1
236492.4650	$34_{6,29}-34_{5,30}$	377.6	1.53e-05	140	0.045	-	-	blend
236683.7060	$17_{9,9}-17_{8,10}$	331.0	1.49e-05	70	0.030	-	-	2.1
236759.6870	$19_{5,15}-18_{5,14}$	129.6	1.86e-04	78	1.679	yes	yes	20.6
237056.9149	$41_{10,32}-40_{11,29}$	763.9	1.38e-06	170	0.000	-	-	blend
237057.1470	$9_{5,4}-8_{4,4}$	230.6	1.69e-05	38	0.037	-	-	2.1
237879.9308	$17_{6,12}-17_{4,13}$	114.6	1.02e-06	70	0.009	-	-	2.3

Notes. Same as Table B.1 but for CH_3OCHO and corresponding to Fig. B.6.

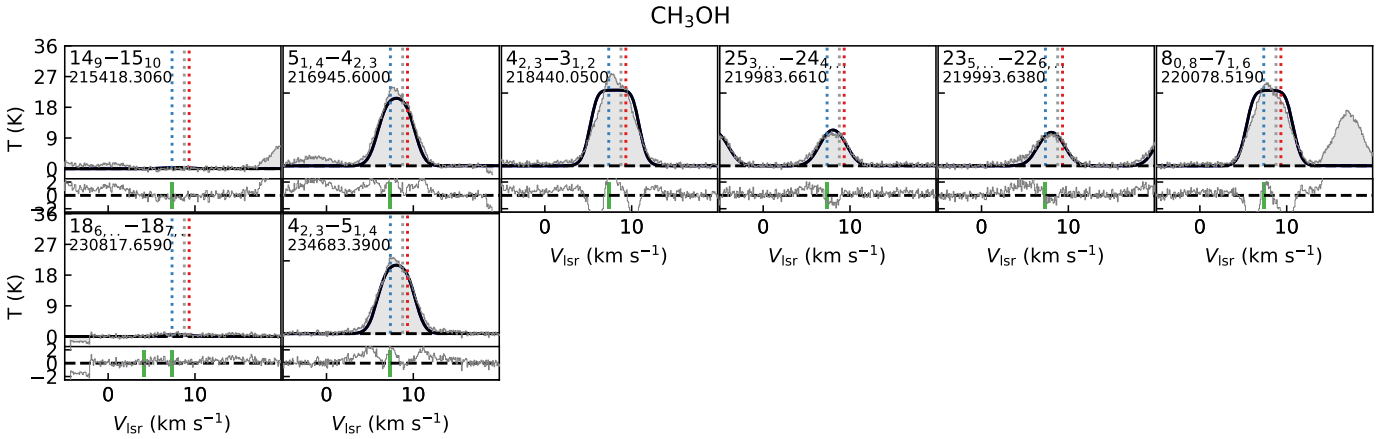

Fig. B.1. Modeled CH_3OH line profiles overlaid on the observed spectra. The three vertical dashed lines show the central velocities of VLA4A (blue), VLA4B (red), and the circumbinary system (gray). The subpanel at the bottom shows the residual from the best fit. The green bars mark the velocities of VLA4A (7.36 km s^{-1}) for all transitions used in the model of CH_3OH.

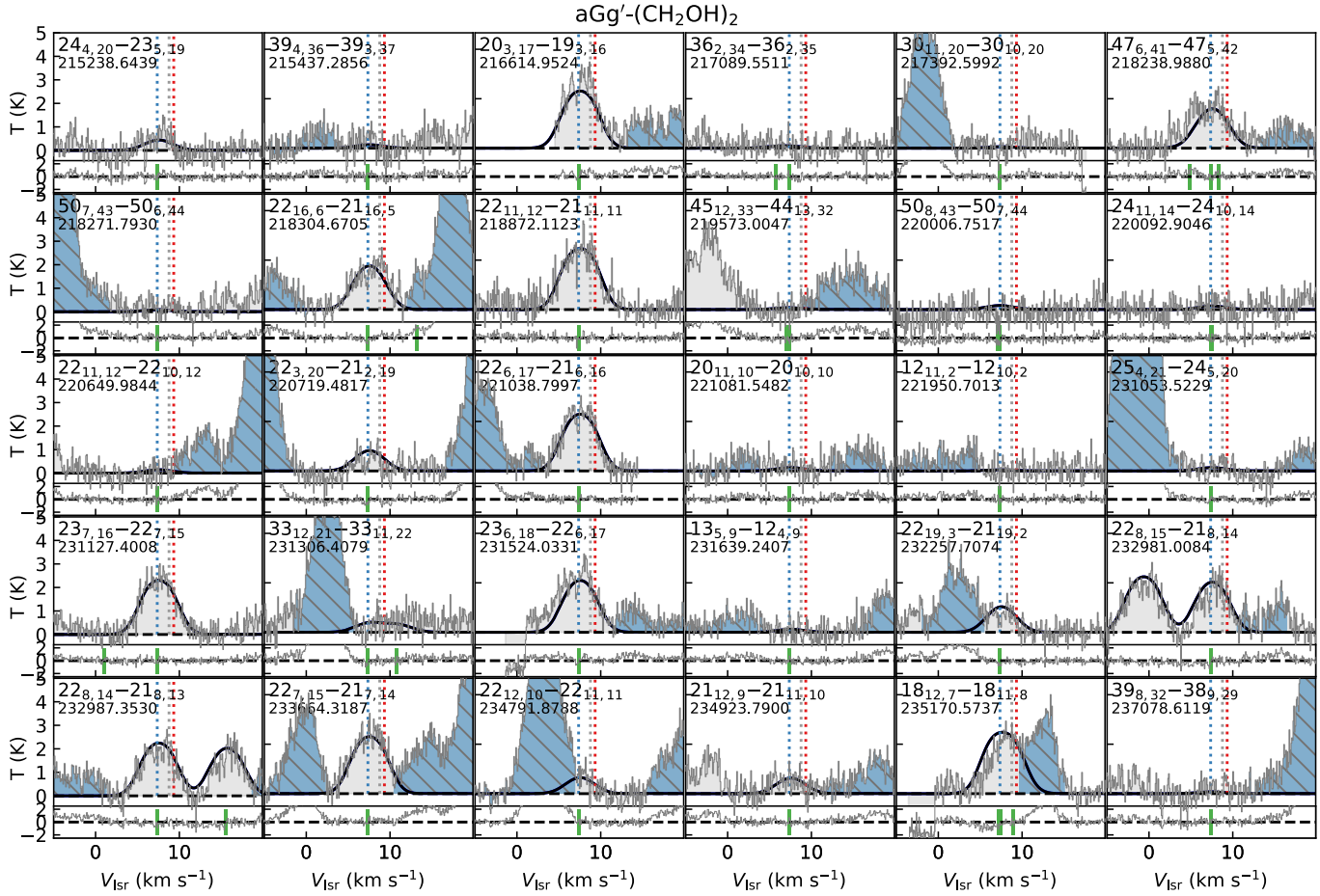

Fig. B.2. Same as Fig. B.1 but for aGg'-$(CH_2OH)_2$. The hatch indicates the regions that are masked for the fitting.

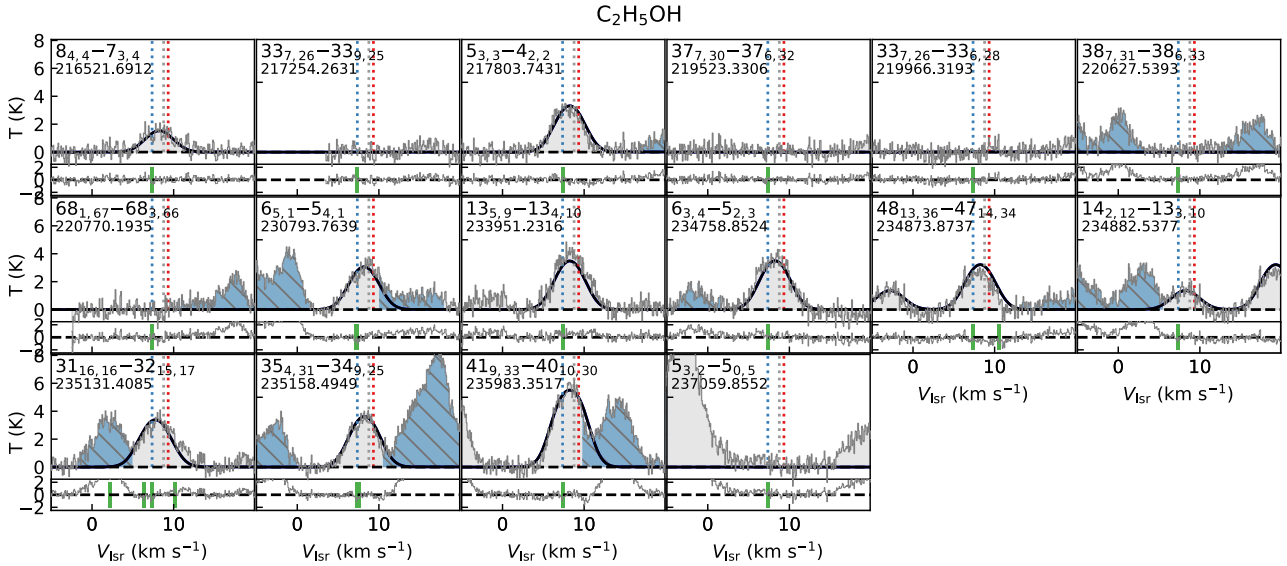

Fig. B.3. Same as Fig. B.2 but for C_2H_5OH.

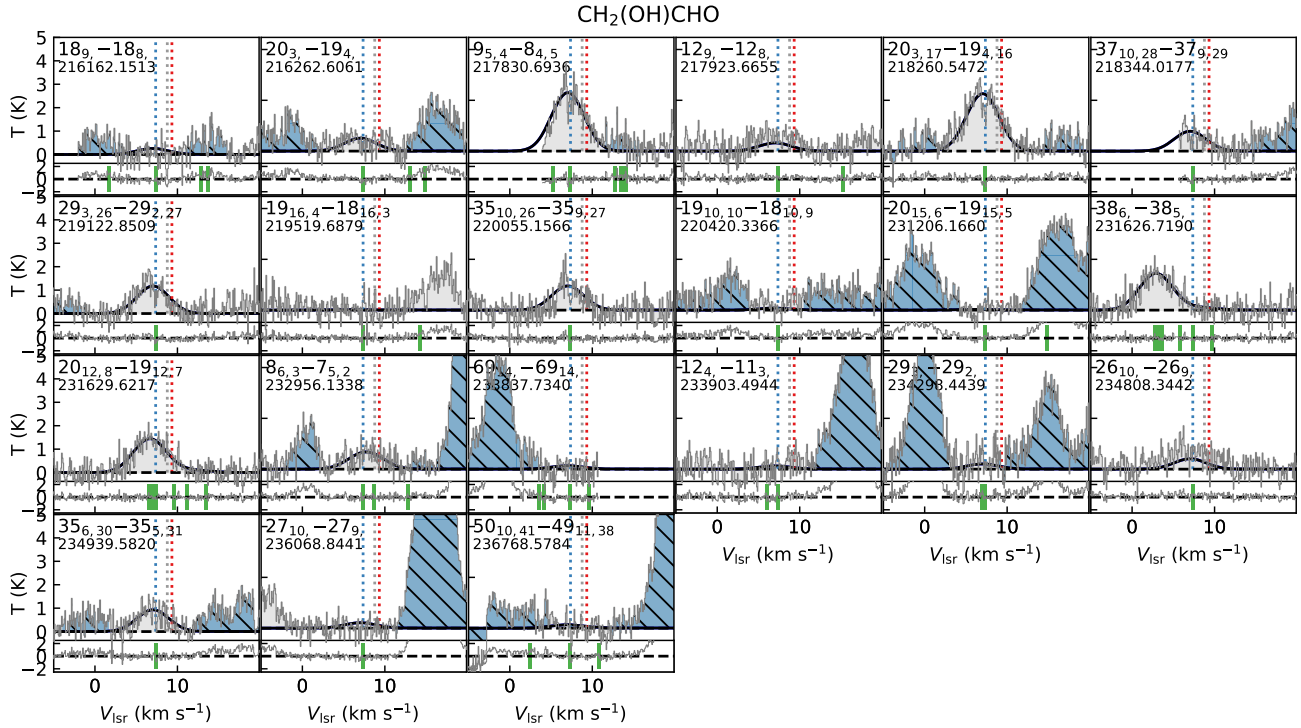

Fig. B.4. Same as Fig. B.2 but for $CH_2(OH)CHO$.

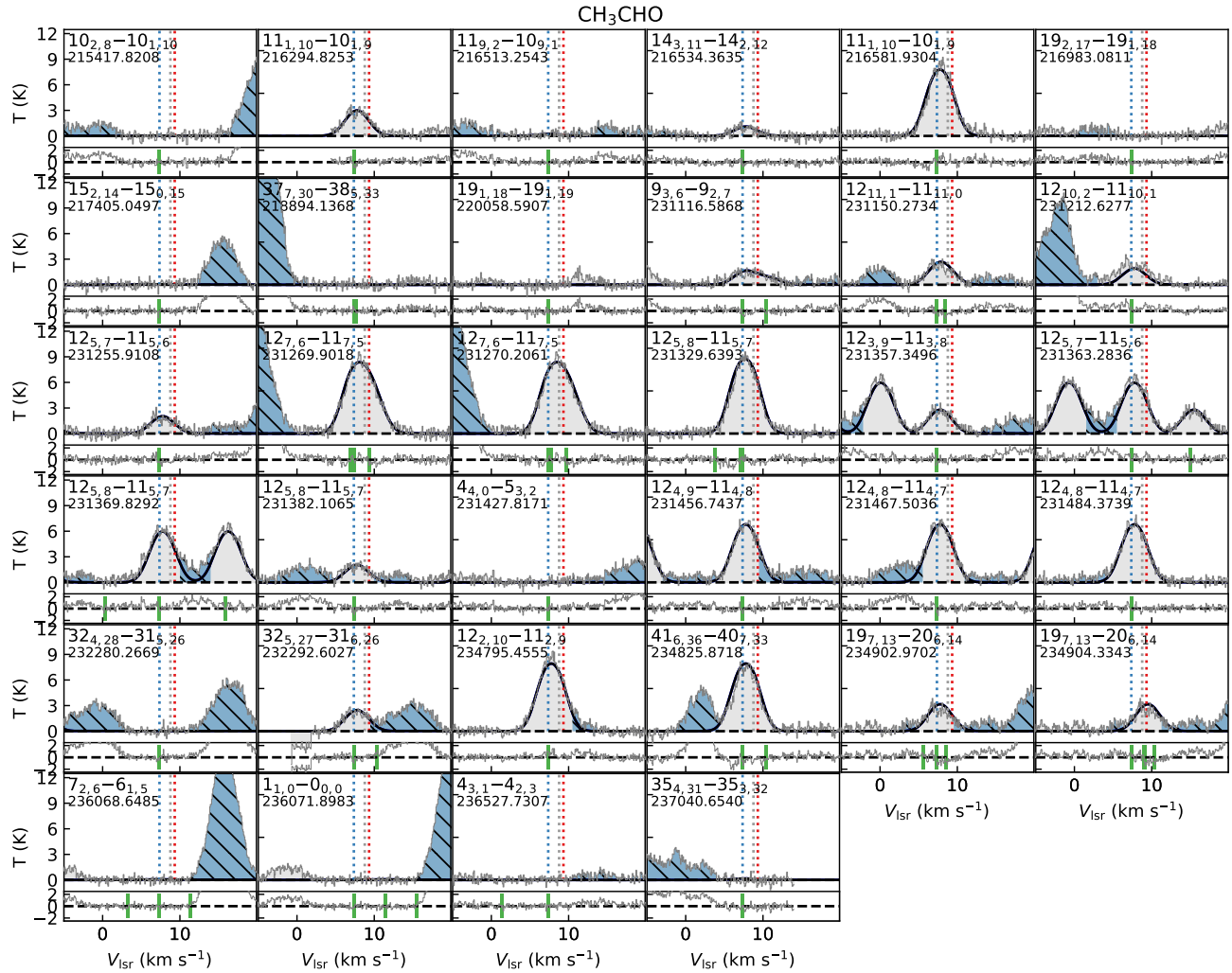

Fig. B.5. Same as Fig. B.2 but for CH_3CHO.

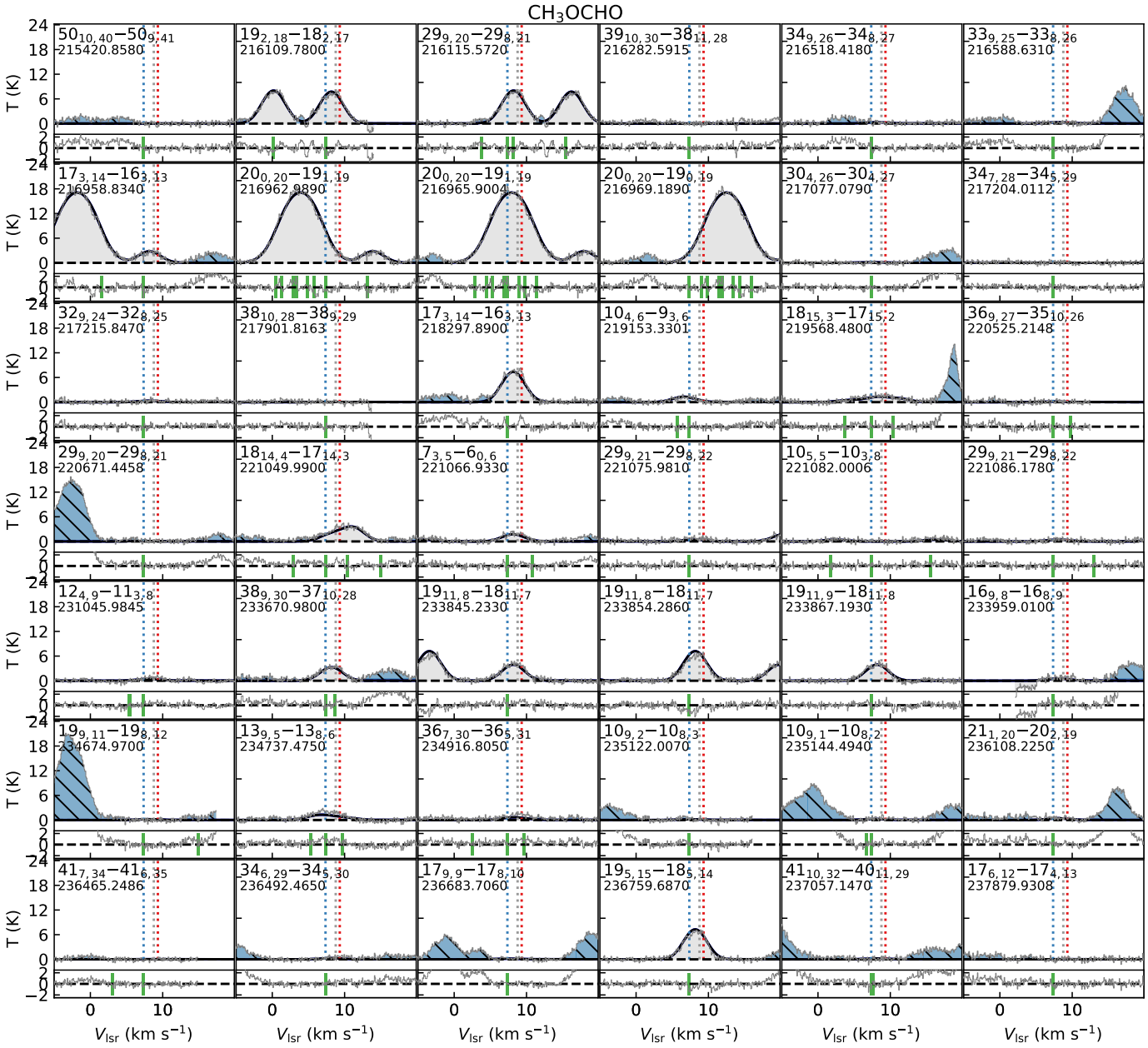

Fig. B.6. Same as Fig. B.2 but for CH_3OCHO.

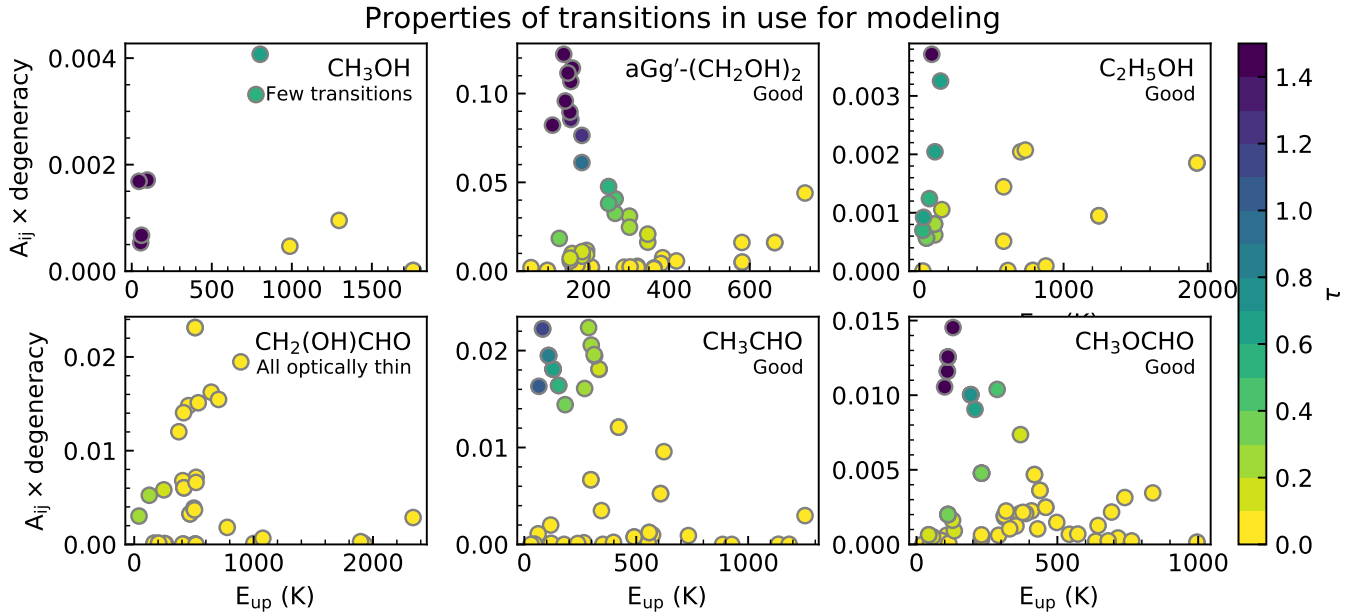

Fig. B.7. Properties of the transitions in use for the modeling. The color of the data points indicates the optical depth for each transition from the single velocity component model. The label "Good" indicates that the energy levels are well sampled by the transitions, allowing us to derive the temperature, and that they cover optically thick emission, allowing us to derive the source size.

Appendix C: CH_3OCH_3

CH_3OCH_3 is detected in the narrowband high-resolution data in only a few transitions without contamination from other lines (Fig. C.1). The only detection with high S/N ratio, $7_{2,5} - 6_{1,6}$, is blended by other transitions so that we cannot analyze the kinematics like in Figs. 3 and 5. One-component LTE fitting is conducted, yielding a source with T_{ex} = 173 K, V_{lsr} = 9.1 km s^{-1}, and FWHM= 2.71 km s^{-1}. The source size and column density is not well constrained given all optically thin ($\tau < 0.2$) line emission. CH_3OCH_3 and CH_3OCHO are considered to be chemically linked (for example Coletta et al. 2020). The one-component models do not provide the same temperature and V_{lsr}, but this could simply be due to the very limited number of transitions available in the case of CH_3OCH_3.

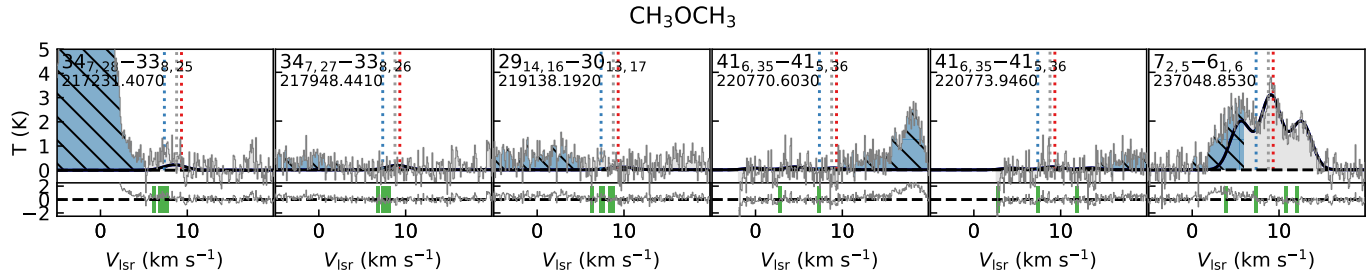

Fig. C.1. Same as Fig. B.2 but for CH_3OCH_3.